Available online at www.sciencedirect.com
ScienceDirect
Comput. Methods Appl. Mech. Engrg. 313 (2017) 53–84
Computer methods in applied mechanics and engineering
www.elsevier.com/locate/cma

A multiscale Implicit Level Set Algorithm (ILSA) to model hydraulic fracture propagation incorporating combined viscous, toughness, and leak-off asymptotics

E.V. Dontsov[a,*], A.P. Peirce[b]

[a] *Department of Civil and Environmental Engineering, University of Houston, Houston, TX, 77204, USA*
[b] *Department of Mathematics, University of British Columbia, Vancouver, British Columbia, V6T 1Z2, Canada*

Received 15 June 2016; received in revised form 6 September 2016; accepted 16 September 2016
Available online 29 September 2016

Highlights

- An implicit level set algorithm (ILSA) for planar hydraulic fractures is developed.
- The ILSA scheme is able to capture multiscale behavior on a coarse rectangular mesh.
- Effects of fracture toughness, fluid viscosity, and leak-off are included.
- The ILSA scheme solution has been validated against a radially symmetric solution.
- The ILSA scheme is used to model hydraulic fractures in three stress layer geometry.

Abstract

This study uses an Implicit Level Set Algorithm (ILSA) to model the propagation of planar hydraulic fractures in situations when their progress is determined by an interplay of fluid viscosity, rock fracture toughness, and fluid leak-off into the formation. One of the key features of our approach is the use of the three-process tip asymptotic solution both as a propagation condition and to capture the multiscale behavior in a weak sense. Using this special tip asymptote is necessary because the validity region of the classical square root fracture opening solution (stemming from linear elastic fracture mechanics) is often limited to a small zone near the fracture tip, which can only be captured by a very fine mesh. In addition, this validity zone depends on the velocity of fracture propagation, so that slow and fast portions of the fracture front may experience different near-tip behavior. The multiscale tip asymptotic solution, on the other hand, has an increased validity region, which makes it possible to capture the near-tip multiscale behavior on a coarse mesh and yields a computationally efficient algorithm. The presence of leak-off also complicates the model considerably as it involves a delay term containing the trigger time history, which depends on the earlier fracture front positions. Moreover, the leak-off from tip elements in which the fracture front speed changes significantly requires special treatment. This three-process asymptotic solution is used to solve the fully coupled integro-delay-PDE model for a propagating planar hydraulic fracture by using a level set algorithm in conjunction with the tip asymptotic solution to locate the moving fracture front and to capture multiscale behavior. Firstly, the developed algorithm is validated against a reference solution for an axisymmetric hydraulic fracture. Secondly, a set of numerical examples involving three stress layers is presented to illustrate the variation of the multiscale near-tip behavior along the fracture perimeter and the need to use the multiscale asymptotic solution in a hydraulic fracturing simulator.

* Corresponding author.
E-mail address: edontsov@central.uh.edu (E.V. Dontsov).

http://dx.doi.org/10.1016/j.cma.2016.09.017

Keywords: Hydraulic fracture; Level set methods; Multi-scale phenomena; Stress jumps; Leak-off

1. Introduction

Hydraulic fractures (HF) are cracks that are produced by the injection of a viscous fluid into a solid medium. HF occur in nature as kilometers-long vertical dikes that bring magma from deep underground chambers through the rock to the earth's surface driven by buoyancy [1–7], or as fluid-filled cracks in glaciers [8]. The most common industrial application of HF is in the stimulation of oil and gas reservoirs to enhance the recovery of hydrocarbons by the creation of permeable pathways, see e.g. [9]. In addition, HF are used for accelerating the waste remediation process [10], waste disposal [11], and preconditioning in rock mining [12].

Apart from buoyancy-driven HF studies most HF models cater for petroleum applications. One of the first models developed was the Khristianovich–Zheltov–Geertsma–De Klerk (KGD) model [13], in which a line fracture propagates under plane strain elastic conditions. Another early model is the Perkins–Kern–Nordgren (PKN) model [14,15], in which a vertical planar fracture with fixed height propagates horizontally. Later, the pseudo-3D (P3D) model was developed [16] as an extension of the PKN model that allows for height growth. There are several variations of the P3D model, including the cell-based P3D model [16], the lumped P3D model [17], the stacked height P3D model [18], and the enhanced P3D model [19]. To overcome the simplifications of the P3D models, more accurate, but less computationally efficient, fully planar 3D models have also been developed [20–22], see also [23] for a review of planar HF simulators. In addition, the special case of an axisymmetric or radial fracture geometry has been extensively studied, and [24] presents a thorough review of the findings. Recently, research effort has shifted towards fully 3D HF modeling [25,26], modeling of simultaneous propagation of multiple HF [27–29], and the interaction of HF with a natural fracture network [30]. A recent review of current HF models can be found in [31].

All HF models include elasticity calculations to ensure equilibrium of the rock, a balance of input fluid volume with stored and leak-off volume, and a propagation criterion to advance the fracture front. In conventional HF modeling a number of different approaches have been used to solve the elastic equilibrium equations, including: the displacement discontinuity method [22], the finite element method [32], and the extended finite element method [33], see also a review paper [34]. More recently a class of phase-field or smeared crack models has been developed, in which fractures are not modeled explicitly but rather by distributed damage that is represented by a field variable [35–37]. In addition, discrete HF models have been developed that treat the solid as a collection of particles in a lattice connected by springs [38,39], or as a collection of particles that interact with each other within a given radius [40]. The primary advantage of both phase-field and discrete models is that they are able to capture the evolution and interaction of complex fracture geometries with significantly less effort than the conventional models in which cracks are modeled explicitly. On the other hand, due to the discrete nature of lattice models and the smeared-out damage representation of cracks by the phase-field approach, it is not clear whether these methodologies will be able to capture the complex multiscale behavior characteristic of HF when multiple physical processes compete to determine their evolution. The other essential component in an HF model involves capturing the fluid flow, which is often taken to be laminar and the fluid is assumed to be Newtonian. More complex HF fluid models consider power-law fluids [41], turbulent fluid flow [8,42], or proppant transport [23,43], in which case the fluid flow equation is modified. This study utilizes the displacement discontinuity method commonly used in HF modeling and assumes laminar fluid flow of a Newtonian fluid within the crack to illustrate the multiscale methodology we have developed to capture the evolution of planar HF. This methodology can also be extended to non-planar and more complex fractures, however this is beyond the scope of this work and left for future research.

Many HF models use a propagation condition based solely on the linear elastic fracture mechanics of a mode I fracture in which the fracture propagates if the stress intensity factor has reached a critical value known as the fracture toughness. However, an analysis of the tip region of a hydraulic fracture [44] indicates that the validity region of the classical square root solution is limited to a small region in the vicinity of the crack tip. Thus, either a very fine mesh is needed to capture the square root behavior near the tip sufficiently accurately, or a special asymptotic solution should be utilized, which incorporates the near tip behavior beyond the square root solution. Recognizing the significance

of the tip region and its rich multiscale behavior, numerous studies have addressed the asymptotic behavior of HF in the near tip region [45–48,44,49]. The use of such a multiscale tip asymptotic solution as a propagation condition within an HF simulator leads to a more accurate numerical solution that is able to capture the multiscale tip behavior on a relatively coarse mesh. However, the implementation of a multiscale tip asymptote is complex and progress has been limited. The tip asymptote without leak-off has been implemented into an enhanced P3D model [50], in which a global approximation for the two-process toughness–viscosity tip asymptote was used. In the context of planar fractures, an Implicit Level Set Algorithm (ILSA) [22] provides a suitable platform for the implementation of any tip asymptotic solution for a planar fracture geometry. This approach has been used to incorporate the tip asymptote that assumes no leak-off in [51], in which a one dimensional interpolation of the numerically calculated and tabulated values for the two-process toughness–viscosity tip asymptote was used. The three-processes tip asymptote that captures fracture toughness, fluid viscosity, and leak-off has been implemented into a simulator for a radial HF in [52] using two-dimensional interpolation of the numerically calculated tip solution obtained in [44]. While two dimensional interpolation of the three-process asymptote is feasible for the symmetric case of a radial fracture, which is a one dimensional problem with a single tip element, such an interpolation scheme becomes extremely costly in the context of arbitrary planar fractures with many distinct elements in the tip region close to the fracture front. However, an accurate closed form approximation for the universal three-processes multiscale tip asymptotic solution that accounts for leak-off was recently obtained in [49]. This development has made it possible to devise an efficient implementation of the three-processes multiscale near tip behavior into an HF simulator that avoids interpolation. It should be noted that including the effect of leak-off not only requires the use of the three-process asymptotic solution, but also complicates the model considerably as it involves a delay term containing the trigger time history, which depends on the previous fracture front positions since the hydraulic fracture initiated. In addition, the rigorous treatment of the leak-off from tip elements in which the fracture front speed changes significantly (e.g. when the fracture traverses a stress barrier) has required the development of a specialized integration procedure to treat the singular leak-off term using the front velocity history. In summary, the aim of this study is to develop an algorithm that is able to solve the delay-integro-PDE model for a single planar HF that is able to incorporate the three-process tip behavior (stemming from the combined interplay of fracture toughness, fluid viscosity, and leak-off) using a relatively coarse mesh.

The paper is organized as follows. Section 2 describes the mathematical model for hydraulic fracture propagation, which outlines the primary assumptions and formulates the governing equations adopted in this study. Section 3 provides a motivation for using the multiscale tip asymptotic solution as a propagation condition for developing a more accurate numerical algorithm and also briefly summarizes the closed form approximate solution for the multiscale tip asymptote that was previously obtained in [49]. Section 4 contains details of the numerical algorithm, which describes the numerical scheme for solving the governing equations presented in Section 2 together with the propagation condition that is based on the multiscale tip asymptote outlined in Section 3. Finally, Section 5 presents numerical results that validate the algorithm developed in this paper against a reference solution and provides a set of numerical examples for a planar hydraulic fracture that illustrate the importance of using the multiscale tip asymptotic solution for HF modeling.

2. Mathematical model

2.1. Assumptions

In order to describe the mathematical model that we use for hydraulic fracturing, we first outline the assumptions that are used to simplify the analysis. The governing equations for describing the propagation of a hydraulic fracture should account for the dominant physical processes that occur in the reservoir during treatment. In particular, they should be able to account for the deformation of the rock caused by the presence of the fracture, incorporate the mechanism for fracture growth, capture the fluid flow inside the crack, and quantify the fluid leak-off into the surrounding porous formation. In order to moderate the complexity of the model, it is assumed that:

(1) There is a single planar (i.e. it is contained in a single plane, see Fig. 1) hydraulically induced fracture and no other (natural) fractures.
(2) The rock is a linear elastic material and is characterized by its Young's modulus E and Poisson's ratio ν.

(3) The fracture growth is governed by linear elastic fracture mechanics (LEFM), see e.g. [53]. Only mode I fracture is considered and the associated rock fracture toughness is denoted by K_{Ic}.
(4) The fluid flow follows lubrication theory, while the fluid is assumed to be incompressible and Newtonian (with a dynamic viscosity μ).
(5) The leak-off is described by Carter's model [54], which assumes one-dimensional diffusion in the direction perpendicular to the fracture surfaces, includes filter cake formation, and is quantified by a single leak-off coefficient C_L.
(6) The rock is assumed to be homogeneous (i.e. the fracture toughness K_{Ic}, Young's modulus E, Poisson's ratio ν, and leak-off coefficient C_L are all spatially constant).
(7) The effect of gravity (i.e the hydrostatic pressure change in the crack) is neglected.
(8) The fluid front coincides with the crack front, since the lag between the two fronts is negligible under the typical high confinement conditions encountered in reservoir stimulation [47,55,56].

Note that it is possible to relax the assumption that K_{Ic} and C_L are homogeneous as well as add the effect of hydrostatic pressure without any significant changes to the algorithm. At the same time, if different fluids are used during the same treatment, or if one desires to account for the effect of proppant, it is also possible to incorporate the heterogeneous viscosity without excessive modifications. Developing a similar algorithm for fluids with different rheology is more challenging, as this requires the corresponding asymptotic solution for the tip region, which, ideally, should be given in closed form for efficient calculations. The assumption that the elastic properties are uniform is also more difficult to overcome since the displacement discontinuity method is utilized to calculate the elastic response of the rock numerically. However, an efficient multi-layer algorithm can be implemented by replacing the Green's function matrix elements for a homogeneous elastic medium by those for a layered elastic medium (see for example [57–59]). Representing a heterogeneous solid medium can be incorporated relatively easily by a finite element method or an extended finite element method, however care is required when incorporating the tip asymptote behavior in these algorithms [33]. Finally, it should also be noted that the algorithm developed in this paper for a single planar fracture can be extended to multiple fractures that propagate along the predefined directions by including elastic interactions between the fractures.

In order to specify the geometry of the problem, in this paper we will focus on the case when a primary layer with height H is sandwiched between two layers with different far-field compressive stresses. In this situation, there are three layers in total and their compressive stresses are denoted by σ_i^h, $i = 1, 2, 3$, as indicated in Fig. 1. Perfect bonding is assumed between the layers. The wellbore (modeled as a point source) coincides with the origin of the (x, y) coordinate system and is located in the middle of the central layer. It is important to note that while the three layers are assumed to have different compressive stresses, the elastic properties, fracture toughness, and leak-off coefficient of all three layers are assumed to be identical. Extension to a layered solid medium with different toughness and leak-off properties in each layer is possible provided the algorithm is adapted to treat the fracture growth near the layer interfaces. While it is possible to derive a Green's function for an elastic material with bonded layers [57,58], the tip asymptote required to capture the transition between two bonded layers with distinct elastic properties has yet to be determined. Finally, the inclusion of an arbitrary variation of the far-field compressive stress $\sigma^h(x, y)$ can be incorporated without noticeable changes to the algorithm.

2.2. Governing equations

This section outlines the governing equations of the mathematical model for a single planar hydraulic fracture that are consistent with the assumptions summarized in the previous section. The (x, y) coordinate system is defined in the plane that contains the fracture, where a source with intensity $Q(t)$ is located at the origin, see Fig. 1. The primary quantities of interest in a hydraulic fracture problem are the time histories of the fracture width $w(x, y, t)$ (fracture opening is in the out-of-plane direction), the fluid pressure $p(x, y, t)$, the fluid flux $\mathbf{q}(x, y, t)$, and the position of the front $\mathcal{C}(t)$. The solution depends on the volumetric injection rate $Q(t)$, the far-field compressive stress σ_i^h, $i = 1, 2, 3$, (perpendicular to the fracture plane), and the four material parameters μ', E', K', and C' defined as

$$\mu' = 12\mu, \qquad E' = \frac{E}{1-\nu^2}, \qquad K' = 4\left(\frac{2}{\pi}\right)^{1/2} K_{Ic}, \qquad C' = 2C_L. \tag{2.1}$$

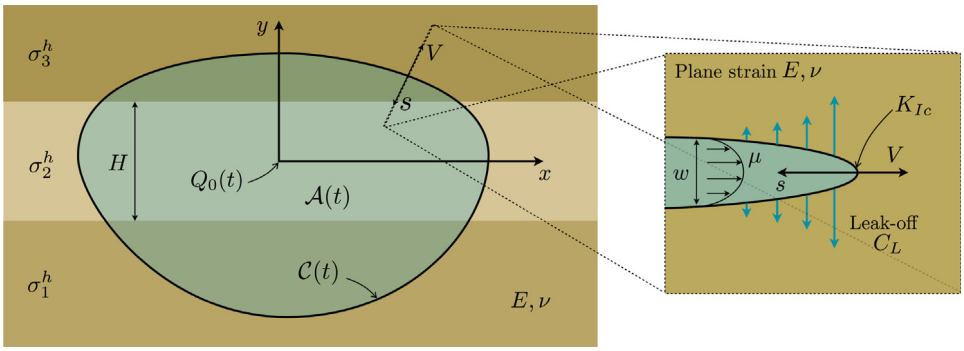

Fig. 1. Left picture shows the schematics of a planar fracture with a footprint $\mathcal{A}(t)$ inscribed within the curve $\mathcal{C}(t)$. The point source with intensity $Q(t)$ is located at the origin of the (x, y) coordinate system. The normal velocity of the front is denoted by V, while s signifies the distance from the fracture tip. A geometry with three layers is considered, where the far-field compressive stress varies from one layer to another. Right picture shows the fracture aperture variation in the near tip region.

Here E' is the plane strain modulus, and μ' is the scaled fluid viscosity, while K' and C' are the scaled fracture toughness and leak-off coefficient respectively. These scaled quantities are introduced to keep equations uncluttered by numerical factors. The front $\mathcal{C}(t)$, and the field quantities $w(x, y, t)$, $p(x, y, t)$, and $\mathbf{q}(x, y, t)$ are governed by a set of equations arising from linear elastic fracture mechanics, lubrication theory, conservation of fluid volume, and the associated boundary conditions that are described next.

2.2.1. Elasticity

In view of the rock homogeneity and linear elasticity assumptions, the elasticity equation that relates the fracture aperture w to the compressive stress field along the crack (which is related to the fluid pressure p) can be condensed into a single hypersingular integral equation [60,61]

$$p(x, y, t) = \sigma^h(y) - \frac{E'}{8\pi} \int_{\mathcal{A}(t)} \frac{w(x', y', t)\mathrm{d}x'\mathrm{d}y'}{\left[(x' - x)^2 + (y' - y)^2\right]^{3/2}}, \tag{2.2}$$

where $\mathcal{A}(t)$ denotes the fracture footprint, i.e. the area enclosed by the crack front $\mathcal{C}(t)$ (see Fig. 1) and $\sigma^h(y)$ is the prescribed *in-situ* geological stress field, which for the three layer system considered in this paper can be written as

$$\sigma^h(y) = \sigma_2^h + (\sigma_3^h - \sigma_2^h)\mathcal{H}\left(y - \tfrac{1}{2}H\right) + (\sigma_1^h - \sigma_2^h)\mathcal{H}\left(-y - \tfrac{1}{2}H\right),$$

where $\mathcal{H}$ denotes Heaviside step function and σ_i^h $(i = 1, 2, 3)$ are the values of the compressive stress in the three considered layers, as shown in Fig. 1.

2.2.2. Lubrication

Utilizing the assumptions that the fracturing fluid is Newtonian and that the flow is laminar, the fluid flux inside the crack can be calculated based on Poiseuille's law

$$\mathbf{q} = -\frac{w^3}{\mu'}\nabla p, \tag{2.3}$$

where $\nabla = (\partial/\partial x, \partial/\partial y)$ is the gradient operator in the fracture plane. Due to the assumed incompressibility of the fluid, the continuity equation reads

$$\frac{\partial w}{\partial t} + \nabla \cdot \mathbf{q} + \frac{C'}{\sqrt{t - t_0(x, y)}} = Q(t)\delta(x, y), \tag{2.4}$$

where the term involving C' captures fluid leak-off according to Carter's model and $t_0(x, y)$ signifies the time instant at which the fracture front was located at the point (x, y). Eqs. (2.3) and (2.4) can be combined to yield the Reynolds

lubrication equation

$$\frac{\partial w}{\partial t} = \frac{1}{\mu'}\nabla \cdot \left(w^3 \nabla p\right) - \frac{C'}{\sqrt{t - t_0(x, y)}} + Q(t)\delta(x, y). \tag{2.5}$$

Since this study focuses on the case when the fluid front within the fracture and the fracture front coalesce (so there is no fluid-lag), the governing equation (2.5) applies within the whole fracture.

2.2.3. Boundary conditions at the moving front $\mathcal{C}(t)$

In order to describe the fracture front evolution, the boundary conditions at the front $\mathcal{C}(t)$ should be specified. By using the classical LEFM solution for the mode I crack tip [53], the fracture propagation criterion is

$$\lim_{s\to 0} \frac{w}{s^{1/2}} = \frac{K'}{E'}, \quad \text{if } V > 0, \qquad \lim_{s\to 0} \frac{w}{s^{1/2}} = \frac{K'_I}{E'}, \quad \text{if } V = 0, \tag{2.6}$$

where s is the distance to the crack front, V is the normal velocity of the front (see Fig. 1), and K'_I is the unknown scaled stress intensity factor. We note here that the fracture is assumed to be in limit equilibrium as soon as it propagates (i.e. $K'_I = K'$, where K' is the scaled fracture toughness, see (2.1)). At the same time, if the fracture does not propagate, then the stress intensity factor is below the critical value, i.e. $K'_I < K'$. The situation when $V = 0$ corresponds to the case of partial fracture closure near the tip region. Note that complete fracture closure ($K'_I = 0$), in which case the fracture front starts to recede, is beyond the scope of this study.

For the case of coalescent fluid and fracture front the propagation condition (2.6) should be supplemented by a zero flux boundary condition [56] at the fracture tip, which can be written as

$$\lim_{s\to 0} w^3 \frac{\partial p}{\partial s} = 0. \tag{2.7}$$

The evolution of the fracture front $C(t)$ (and the associated normal velocity V) is implicitly determined by Eqs. (2.6) and (2.7).

3. Multiscale tip asymptotic behavior

3.1. Motivation for using a multiscale tip asymptotic solution

The LEFM-based propagation condition (2.6) sets a condition at the fracture tip, which can be used to locate the fracture boundary. However, the validity region of this asymptotic solution is often limited to a small region near the fracture tip (see e.g. [44] for the analysis of the near tip behavior). In other words, in order to resolve the LEFM behavior (2.6) near the fracture tip (within the adopted mathematical model), one would need to use a very fine mesh, which would lead to excessive computational costs. In order to avoid this situation, the LEFM near tip solution for the fracture aperture (2.6) can be replaced by a suitable asymptotic solution with an increased validity region, i.e.

$$w(s) \approx w_a(s), \qquad s \ll L, \tag{3.1}$$

where $w_a(s)$ is the fracture width variation in the near tip region, and L is the characteristic length of the fracture. The meaning of (3.1) is that the fracture aperture should follow the specified solution, $w_a(s)$, in the tip region, where the latter region is defined relative to the characteristic size of the fracture, L. Note that $w_a(s) \to (K'/E')s^{1/2}$ for $s \to 0$, which is in agreement with (2.6), but this limit may not always be reached at the computational length scale even for $s \ll L$, hence the need to use the tip asymptotic solution $w_a(s)$. As can be seen on the right picture in Fig. 1, the near tip solution can be calculated by considering a semi-infinite hydraulic fracture that propagates steadily with a velocity V under plane strain elastic conditions. This property of planar hydraulic fractures was derived rigorously in [22]. In the context of the adopted mathematical model involving all the processes of viscous dissipation, toughness energy release, and leak-off, the problem of a tip region was first analyzed in [44] and then revisited in [49], where both studies clearly establish the multiscale nature of the solution. The following sections are devoted to the problem of the tip region and describe a closed form approximation for $w_a(s)$ that was obtained in [49].

3.2. Problem formulation and vertex solutions

As shown in [22,44], the behavior of the solution in the tip region of a hydraulic fracture is governed by the problem of a semi-infinite hydraulic fracture propagating steadily with the velocity V under plane strain elastic conditions. Consistent with Fig. 1, we introduce a moving coordinate system, in which s denotes the distance from the tip to a point inside the fracture. In this case, the governing equations for the near tip problem can be written as [22,44,49]

$$\frac{w_a^2}{\mu'}\frac{dp_a}{ds} = V + 2C'V^{1/2}\frac{s^{1/2}}{w_a}, \qquad p_a(s) = \frac{E'}{4\pi}\int_0^\infty \frac{dw_a(s')}{ds'}\frac{ds'}{s-s'}, \qquad w_a = \frac{K'}{E'}s^{1/2}, \quad s \to 0, \tag{3.2}$$

where w_a is the fracture width for the semi-infinite crack problem, p_a is the corresponding fluid pressure, V is the fracture propagation velocity, and μ', C', E', and K' are the scaled material properties defined in (2.1). Here the first equation is the integrated fluid balance equation (2.5) that is reduced in the limit to a one-dimensional flow, the elasticity equation (2.2) reduces to the second equation in (3.2), and the third equation is the propagation condition (2.6). Note that (3.2) utilizes an identical mathematical model (and therefore assumptions) as the planar hydraulic fracture problem under consideration, but applies to a different fracture geometry.

A complete asymptotic analysis of the semi-infinite hydraulic fracture problem, governed by (3.2), was performed in [44]. In particular, it is important to note that there are three distinct limiting regimes of propagation, namely, toughness (denoted by k), leak-off (denoted by $\tilde{m}$), and viscous (denoted by m). The fracture width solutions (so-called vertex solutions) for these regimes are respectively given by

$$w_k = \frac{K'}{E'}s^{1/2}, \qquad w_{\tilde{m}} = \beta_{\tilde{m}}\Big(\frac{4\mu'^2VC'^2}{E'^2}\Big)^{1/8}s^{5/8}, \qquad w_m = \beta_m\Big(\frac{\mu'V}{E'}\Big)^{1/3}s^{2/3}, \tag{3.3}$$

where $\beta_{\tilde{m}} = 4/(15^{1/4}(\sqrt{2}-1)^{1/4})$ and $\beta_m = 2^{1/3}3^{5/6}$. The vertex solutions (3.3) represent limiting cases when either toughness, viscosity, or leak-off dominate the response. However, knowledge of the vertex solutions (3.3) is not sufficient since the intermediate behavior between these limiting solutions is not captured. In addition, since the vertex solutions depend on the velocity of crack propagation V, a fracture may change the near tip behavior as the velocity changes.

There are two possibilities for calculating $w_a(s)$. The first entails a numerical solution of (3.2), which is tabulated for a set of parameters and then used in conjunction with interpolation to obtain $w_a(s)$, see [51,52] in which such an approach is used. Alternatively, an accurate closed form approximation for $w_a(s)$, which was obtained in [49], can be used. This study considers the second approach since it leads to a more efficient numerical scheme.

3.3. Approximate solution

3.3.1. Solution in original scaling

In Section 4.2 we describe an iterative algorithm that uses the asymptotic solution (3.1) to locate the unknown fracture front. In particular, given a trial width w_a associated with the current estimate of the front position, the asymptotic relation (3.1) is inverted to determine a new estimate of the distance s to the free boundary. In Section 4.3 we describe how the asymptote (3.1) is integrated over the tip elements in order to capture the multiscale tip asymptotic behavior in a weak sense. Given the fundamental importance of the asymptotic solution (3.1), this section summarizes the solution for a semi-infinite hydraulic fracture with leak-off, which is governed by (3.2). An approximate solution to (3.2) that can be evaluated extremely efficiently was described in detail in [49]. Therefore, in this section we present only the key features that are necessary to reproduce the results, while the details of the procedure for obtaining the solution can be found in [49].

The original solution is written in terms of the following scaled quantities:

$$\tilde{w} = \frac{E'w_a}{K's^{1/2}}, \qquad \chi = \frac{2C'E'}{V^{1/2}K'}, \qquad \tilde{s} = (s/l)^{1/2}, \qquad l = \Big(\frac{K'^3}{\mu'E'^2V}\Big)^2, \tag{3.4}$$

where $\tilde{w}$ is the fracture width normalized with respect to the toughness asymptote, χ is the leak-off parameter, $\tilde{s}$ is the square root of the normalized distance from the fracture tip, while l is the characteristic length scale. For future

reference, it is instructive to note that the vertex solutions (3.3) can be rewritten using (3.4) as

$$\tilde{w}_k = 1, \qquad \tilde{w}_{\tilde{m}} = \beta_{\tilde{m}} \chi^{1/4} \tilde{s}^{1/4}, \qquad \tilde{w}_m = \beta_m \tilde{s}^{1/3}. \tag{3.5}$$

As follows from [49] the zeroth-order approximate solution can be written implicitly as

$$\tilde{w}_0^3 - 1 - \frac{3}{2} b_0 (\tilde{w}_0^2 - 1) + 3 b_0^2 (\tilde{w}_0 - 1) - 3 b_0^3 \ln\Big(\frac{b_0 + \tilde{w}_0}{b_0 + 1}\Big) = \beta_m^3 \tilde{s}, \qquad b_0 = \frac{3\beta_{\tilde{m}}^4}{4\beta_m^3} \chi \approx 0.9912\, \chi. \tag{3.6}$$

This zeroth-order approximation captures all vertex solutions (3.5) precisely in the limiting cases, while the error in the transition regimes does not exceed 1.1%. To obtain the so-called δ-correction, it is assumed that $\tilde{w} \propto \tilde{s}^{\delta}$, where the power δ is computed on the basis of (3.6) as

$$\delta = \frac{\tilde{s}}{\tilde{w}_0} \frac{d\tilde{w}_0}{d\tilde{s}} = \frac{\beta_m^3 \tilde{s}(\tilde{w}_0)}{3\tilde{w}_0^3} \Big(1 + \frac{b_0}{\tilde{w}_0}\Big), \qquad 0 \leqslant \delta \leqslant 1/3. \tag{3.7}$$

The latter values of δ from (3.7) are substituted into

$$\tilde{w}_\delta^3 - 1 - \frac{3}{2} b (\tilde{w}_\delta^2 - 1) + 3 b^2 (\tilde{w}_\delta - 1) - 3 b^3 \ln\Big(\frac{b + \tilde{w}_\delta}{b + 1}\Big) = 3 C_1(\delta) \tilde{s}, \qquad b = \frac{C_2(\delta)}{C_1(\delta)} \chi, \tag{3.8}$$

where

$$C_1(\delta) = \frac{4(1 - 2\delta)}{\delta(1 - \delta)} \tan(\pi\delta), \qquad C_2(\delta) = \frac{16(1 - 3\delta)}{3\delta(2 - 3\delta)} \tan\Big(\frac{3\pi}{2}\delta\Big). \tag{3.9}$$

The solution $\tilde{w}(\tilde{x}, \chi)$ is implicitly defined by (3.7)–(3.9), and the scaling (3.4) can be used to obtain unscaled results. It is shown in [49] that the error introduced by the approximation (3.8) does not exceed 0.14% for a wide range of parameters that captures all transition regions (note that the vertex solutions (3.5) are captured precisely). A description of the multiscale behavior of the solution $w_a(s)$ is beyond the scope of this study and can be found in [44,49], while, at the same time, the approximation (3.8) is one of the key components of the numerical scheme for the planar fracture problem since it is used in the multiscale propagation condition (3.1).

3.3.2. Solution in a new scaling

Unfortunately, the original scaling (3.4) prevents us from obtaining a solution directly for the case of a zero fracture toughness, i.e. $K' = 0$ (since $\tilde{w}$ is not defined). This situation may occur when a hydraulic fracture propagates along a pre-existing fracture or between two un-bonded interfaces, so the model should be able to capture this limit. Since the problem is solely concealed by the scaling (3.4), we introduce a different set of variables, namely

$$\hat{K} = \frac{1}{\tilde{w}} = \frac{K' s^{1/2}}{E' w}, \qquad \hat{C} = \frac{\chi}{\tilde{w}} = \frac{2C' s^{1/2}}{V^{1/2} w}, \qquad \hat{s} = \frac{\tilde{s}}{\tilde{w}^3} = \frac{\mu' V s^2}{E' w^3}, \tag{3.10}$$

where $0 \leqslant \hat{K} \leqslant 1$ is related to scaled fracture toughness, $\hat{C} \geqslant 0$ represents the leak-off, and $\hat{s}$ is the scaled s coordinate. Using (3.10), Eq. (3.8) can be rewritten as

$$\hat{s} = \frac{1}{3C_1(\delta)} \Big[1 - \hat{K}^3 - \frac{3}{2} \hat{C}\hat{b}(1 - \hat{K}^2) + 3\hat{C}^2\hat{b}^2(1 - \hat{K}) - 3\hat{C}^3\hat{b}^3 \ln\Big(\frac{\hat{C}\hat{b} + 1}{\hat{C}\hat{b} + \hat{K}}\Big)\Big] \equiv f(\hat{K}, \hat{C}\hat{b}, C_1),$$
$$\hat{b} = \frac{C_2(\delta)}{C_1(\delta)}. \tag{3.11}$$

The zeroth-order approximation (3.6) can be written using the same short-hand notation as in (3.11) as

$$\hat{s} = f\Big(\hat{K}, \frac{3\beta_{\tilde{m}}^4}{4\beta_m^3}\hat{C}, \frac{\beta_m^3}{3}\Big) \equiv g_0(\hat{K}, \hat{C}). \tag{3.12}$$

Eq. (3.7) written in terms of the variables (3.10) transforms to

$$\delta = \frac{\beta_m^3}{3}\Big(1 + \frac{3\beta_{\tilde{m}}^4}{4\beta_m^3}\hat{C}\Big) g_0(\hat{K}, \hat{C}) \equiv \Delta(\hat{K}, \hat{C}). \tag{3.13}$$

By substituting (3.13) into (3.11), the δ-corrected solution (3.8) can be written as

$$\hat{s} = f\Big(\hat{K}, \hat{C}\hat{b}\big(\Delta(\hat{K}, \hat{C})\big), C_1\big(\Delta(\hat{K}, \hat{C})\big)\Big) \equiv g_\delta(\hat{K}, \hat{C}), \tag{3.14}$$

where the functions $C_1(\delta)$ and $\hat{b}(\delta)$ are defined respectively in (3.9) and (3.11). Eq. (3.14) is the definition of the function g_δ, where the latter is essentially equal to the function f defined in (3.11), in which the relations $C_1(\delta)$ and $\hat{b}(\delta)$ are computed using (3.9) and (3.11), and δ is calculated using (3.13). Clearly, the formulation (3.14) permits zero values of the fracture toughness $K' = 0$, since it corresponds to the case $\hat{K} = 0$ and the function $g_\delta(0, \hat{C})$ is well-defined. It should be noted here that the function g_δ is defined for $0 \leqslant \hat{K} \leqslant 1$ and $\hat{C} \geqslant 0$. The situations in which $\hat{K} < 0$ or $\hat{C} < 0$ are not physical, however it is possible to encounter a situation in which $\hat{K} > 1$. The case $\hat{K} > 1$ corresponds to the situation when the stress intensity factor is below the fracture toughness, in which case the fracture does not propagate, as indicated in (2.6). To impose this condition, the function g_δ is set to zero for $\hat{K} > 1$ and w_a is set to the toughness solution with an unknown stress intensity factor K', in which case (3.14) can be expressed in dimensional form using (3.10) as

$$\begin{aligned} &\frac{s^2 V \mu'}{E' w_a^3} = g_\delta\Big(\frac{K' s^{1/2}}{E' w_a}, \frac{2 s^{1/2} C'}{w_a V^{1/2}}\Big), && \frac{K' s^{1/2}}{E' w_a} \leqslant 1 \quad \text{and} \quad V \geqslant 0, \\ &w_a = \frac{K_I' s^{1/2}}{E'}, && \frac{K' s^{1/2}}{E' w_a} > 1 \quad \text{and} \quad V = 0, \end{aligned} \tag{3.15}$$

where K_I' is the unknown scaled stress intensity factor (note a notation difference between the stress intensity factor K_I' and the fracture toughness K').

Eq. (3.15) provides an approximate implicit closed-form solution for the fracture aperture variation in the tip region $w_a(s)$ that is described in (3.1). The latter solution captures all limiting solutions (3.3) together with all possible transition regions, see [49] for more details. Note here that g_δ is a relatively simple function, so that a numerical evaluation of the solution through the implicit relation (3.15) is computationally efficient, as compared to a numerical solution of (3.2) combined with interpolation. Once the solution is obtained from (3.15), it is then used in the numerical scheme for the whole fracture to impose the propagation condition (3.1).

3.3.3. *Moments of the solution*

As will be shown later, the numerical algorithm for a planar hydraulic fracture requires not only the asymptotic solution $w_a(s)$, but its zeroth (fracture volume) and first moments. By using the fact that $\tilde{w} \propto \tilde{s}^\delta$ together with the scaling (3.4), and the fact that δ varies slowly, these moments can be expressed as

$$M_0(s) = \int_0^s w_a(s')\, ds' \approx \frac{2\, w_a(s) s}{3 + \delta}, \qquad M_1(s) = \int_0^s w_a(s') s'\, ds' \approx \frac{2\, w_a(s) s^2}{5 + \delta}. \tag{3.16}$$

Since $0 \leqslant \delta \leqslant 1/3$ (which can be seen from (3.5)), even a constant approximation $\delta = 1/6$ leads to an error of only 5% for M_0 and 3% for M_1. To decrease these errors, one may use (3.13) to calculate $\delta = \Delta(\hat{K}, \hat{C})$ for given values of $\hat{K}$ and $\hat{C}$. This reduces the error in the approximation for M_0 to 1%, and that for M_1 to 0.4%. To achieve an even better approximation, one needs to use the value of δ at a point inside the interval $[0, \tilde{s}]$. One possibility is to use a Taylor series expansion of (3.7) to obtain

$$\delta(\tilde{s}(1-p)) \approx \big(1 - p + p\, g_0(\hat{K}, \hat{C})(\beta_m^3 + \beta_{\tilde{m}}^4 \hat{C})\big)\Delta(\hat{K}, \hat{C}) \equiv \Delta_p(\hat{K}, \hat{C}, p), \tag{3.17}$$

where $0 \leqslant p \leqslant 1$ is a parameter. By substituting (3.17) into (3.16), we can express the moments as

$$M_0(s) = \frac{2\, w_a(s) s}{3 + \Delta_p(\hat{K}, \hat{C}, p_0)}, \qquad M_1(s) = \frac{2\, w_a(s) s^2}{5 + \Delta_p(\hat{K}, \hat{C}, p_1)}, \tag{3.18}$$

where the function Δ_p is defined in (3.17), and $\hat{K}$ and $\hat{C}$ are evaluated at the point s and are given in (3.10). It is shown through a series of numerical experiments that $p_0 = 0.377$ corresponds to the smallest error of 0.14% for the volume M_0, while $p_1 = 0.260$ corresponds to the smallest error of 0.05% for the first moment M_1. Here the error is computed as a maximum relative discrepancy between the numerical solution (which utilizes numerical integration in (3.16)) and the approximations (3.18). For completeness, it should be noted that the case $V = 0$ in (3.15) is captured by setting $\Delta_p(\hat{K}, \hat{C}, p) = 0$ for $\hat{K} > 1$.

In summary, to implement the propagation condition (3.1) into a planar model the numerical scheme requires the knowledge of the functions g_δ and Δ_p that allow us to calculate the fracture width at a distance s away from the tip $w_a(s)$ using (3.15), as well as the zeroth and first moments of the solution (3.18).

3.4. Parametric triangle

In order to visualize the "position" of the asymptotic solution w_a relative to the vertex solutions (3.3), it is useful to represent w_a as a point in a phase space comprising a parametric triangle (see e.g. [44]) whose vertices represent the three vertex solutions. To draw this triangle in a quantitative manner, let us first introduce shape functions associated with the vertex solutions (3.3) and the universal asymptotic solution w_a (3.15) as follows

$$N_k = \frac{n_k}{n_k + n_m + n_{\tilde{m}}}, \qquad N_{\tilde{m}} = \frac{n_{\tilde{m}}}{n_k + n_m + n_{\tilde{m}}}, \qquad N_m = \frac{n_m}{n_k + n_m + n_{\tilde{m}}}, \tag{3.19}$$
$$n_k = \frac{w_k}{w_a - w_k}, \qquad n_{\tilde{m}} = \frac{w_{\tilde{m}}}{w_a - w_{\tilde{m}}}, \qquad n_m = \frac{w_m}{w_a - w_m}.$$

Note that the values of N_k, $N_{\tilde{m}}$, and N_m are in the interval $[0, 1]$, and that the shape functions satisfy the partition of unity property $N_k + N_{\tilde{m}} + N_m = 1$. By selecting the location of the vertices as $(x_m, y_m) = (0, 0)$, $(x_{\tilde{m}}, y_{\tilde{m}}) = (1/2, \sqrt{3}/2)$, and $(x_k, y_k) = (1, 0)$, a point inside the triangle is determined by

$$x_{\text{tr}} = x_m N_m + x_{\tilde{m}} N_{\tilde{m}} + x_k N_k, \qquad y_{\text{tr}} = y_m N_m + y_{\tilde{m}} N_{\tilde{m}} + y_k N_k. \tag{3.20}$$

In other words, first the shape functions (3.19) are calculated for a given asymptotic solution w_a at point s (note that the vertex solutions in (3.19) are evaluated at the same distance from the tip s), and then the position inside the parametric triangle is determined from (3.20).

It is also useful to fill the parametric triangle with a colormap to be able to indicate the location in phase space at which a given computational element is operating. Thus the elements that utilize the asymptotic solution for tracking the moving fracture front can be colored according to the position of the asymptotic solution inside the parametric triangle. This will enable us to determine the relative position of the asymptotic solution inside the parametric triangle by inspecting the color of the element. To specify the color filling of the triangle, we adopt the RGB color model, in which the intensity of each color component is in the interval $[0, 1]$ and the intensities of the constituent red, green, and blue colors are calculated by using the corresponding values of the shape functions N_k, $N_{\tilde{m}}$, and N_m (3.19), so that $[r, g, b] = [N_k, N_{\tilde{m}}, N_m]$. Fig. 2 shows triangles depicted according to this description. The blue-colored region corresponds to the situation in which the asymptotic solution w_a is close to the viscous asymptote w_m. The green-colored region corresponds to the situation in which the asymptotic solution w_a is close to the leak-off asymptote $w_{\tilde{m}}$. The red-colored region corresponds to the situation in which the asymptotic solution w_a is close to the toughness asymptote w_k. The left panel in Fig. 2 also shows contour lines indicating regions where the vertex solutions (3.5) apply to within either a 4% or 8% error. The right panel in Fig. 2 indicates the trajectories of the semi-infinite fracture solution w_a for different values of the leak-off parameter χ. Each trajectory represents the solution $w_a(s)$ as s varies from 0 to ∞ for a given constant value of χ. All trajectories start at the k vertex (associated with small distances from the tip s) and end at the m vertex (for large values of s). It is important to note that the solution that corresponds to the case $V = 0$ in (3.15) can lie outside of the triangle, but is displayed at the k vertex for convenience.

4. Implementing the universal tip asymptote within the Implicit Level Set Algorithm (ILSA)

4.1. Discrete equations

This study adopts a discretization, in which the (x, y) plane that contains the fracture is tessellated into a fixed uniform rectangular mesh $\cup \mathcal{A}_{m,n}$ as shown in Fig. 3. The elements are centered at (x_m, y_n) and have dimensions Δx

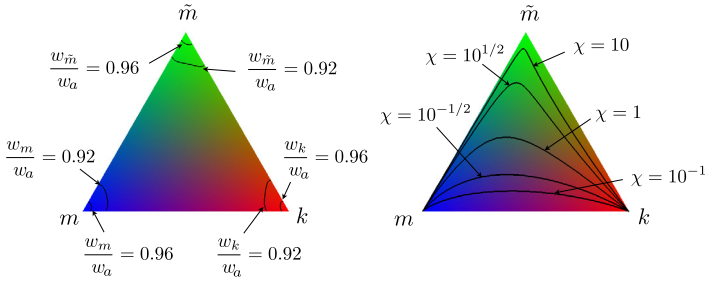

Fig. 2. Left panel: the parametric triangle with contour lines indicating the regions where vertex solutions (3.3) apply to within 4% and 8% error. Right panel: the parametric triangle with the trajectories that correspond to the semi-infinite fracture solution w_a for different values of the leak-off parameter χ. (For interpretation of the references to color in this figure legend, the reader is referred to the web version of this article.)

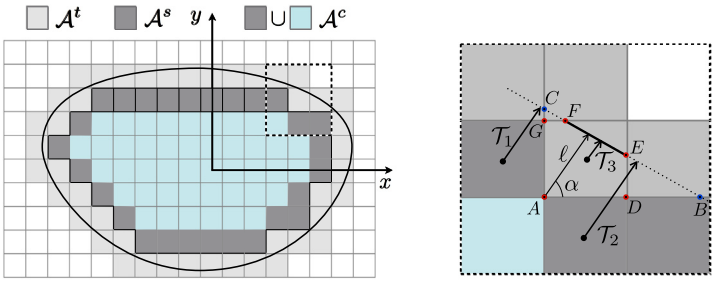

Fig. 3. Left panel: schematics of a hydraulic fracture footprint with mesh, where $\mathcal{A}^t$ are the tip elements, $\mathcal{A}^s$ are the survey elements, and $\mathcal{A}^c$ are the channel elements. Right panel: schematics of the procedure for locating a moving fracture front. (For interpretation of the references to color in this figure legend, the reader is referred to the web version of this article.)

and Δy. The fracture footprint $\mathcal{A}(t)$ is then covered by rectangular elements $\mathcal{A}_{m,n}$ such that $\mathcal{A} \subseteq \cup \mathcal{A}_{m,n}$. Note that this discretization is very similar to the one used in [22,51]. To implement the ILSA scheme it is important to distinguish three different types of elements $\mathcal{A}_{m,n}$ that intersect $\mathcal{A}$, namely the channel, the tip, and the survey elements. The tip elements $\mathcal{A}^t$ are partially filled elements that contain the fracture front $\mathcal{C}$ and are denoted by the light gray color in Fig. 3. The channel elements $\mathcal{A}^c$ are completely filled elements and are indicated by light blue and dark gray coloring in Fig. 3. The survey elements $\mathcal{A}^s$ are a subset of the channel elements $\mathcal{A}^c$ that have at least one common face with a tip element and are indicated by the dark gray coloring in Fig. 3. The survey elements are used to locate the moving fracture front.

A piece-wise constant approximation for the fracture width is employed, so that

$$w(x,y,t) = \sum_{m,n} w_{m,n}(t) H_{m,n}(x,y), \qquad H_{m,n}(x,y) = \begin{cases} 1 \text{ for } (x,y) \in \mathcal{A}_{m,n} \\ 0 \text{ for } (x,y) \notin \mathcal{A}_{m,n}. \end{cases} \tag{4.1}$$

The lubrication equation (2.5), integrated in time from $t - \Delta t$ to t and over the element $\mathcal{A}_{m,n}$, is discretized via the finite volume method to yield

$$w_{m,n}(t) - w_{m,n}(t - \Delta t) = \Delta t \, [\boldsymbol{A}(\boldsymbol{w})\boldsymbol{p}]_{m,n} + S_{m,n}, \tag{4.2}$$

where $S_{m,n}$ is the source/leak-off term and

$$\begin{aligned} [A(\boldsymbol{w})\boldsymbol{p}]_{m,n} = \frac{1}{\Delta x}\left[\frac{w^3_{m+\frac{1}{2},n}}{\mu'} \frac{p_{m+1,n} - p_{m,n}}{\Delta x} - \frac{w^3_{m-\frac{1}{2},n}}{\mu'} \frac{p_{m,n} - p_{m-1,n}}{\Delta x} \right] \\ + \frac{1}{\Delta y}\left[\frac{w^3_{m,n+\frac{1}{2}}}{\mu'} \frac{p_{m,n+1} - p_{m,n}}{\Delta y} - \frac{w^3_{m,n-\frac{1}{2}}}{\mu'} \frac{p_{m,n} - p_{m,n-1}}{\Delta y} \right], \end{aligned} \tag{4.3}$$

where the edge widths are given by $w_{m\pm\frac{1}{2},n} = \frac{1}{2}(w_{m\pm1,n} + w_{m,n})$ and $w_{m,n\pm\frac{1}{2}} = \frac{1}{2}(w_{m,n\pm1} + w_{m,n})$. Zero flux boundary conditions (2.7) are implemented in tip elements by removing the terms associated with the element faces having zero boundary fluxes from the difference operator (4.3). Eq. (4.2) can be expressed on the following succinct form:

$$\boldsymbol{w}(t) = \boldsymbol{w}(t - \Delta t) + \Delta t \boldsymbol{A}(\boldsymbol{w})\boldsymbol{p} + \boldsymbol{S}, \tag{4.4}$$

where $\boldsymbol{w}$ is the vector that contains all width values $w_{m,n}$, $\boldsymbol{p}$ is the vector that contains all pressure values $p_{m,n}$, and $\boldsymbol{S}$ is the vector that contains all the source/leak-off terms $S_{m,n}$. Here $\boldsymbol{A}(\boldsymbol{w})$ and $\boldsymbol{p}$ in (4.4) are evaluated at time t, so that time integration is performed using the backward Euler scheme. This implicit formulation is important to ensure stability when using a relatively large time step. Explicit time integration would require a very small time step since the system (4.4) is very stiff [22].

In order to incorporate the propagation condition (3.1), it is essential to distinguish between the channel and tip elements. In this setting, all the variables can be split as follows:

$$\boldsymbol{w} = [\boldsymbol{w}^c, \boldsymbol{w}^t], \qquad \boldsymbol{p} = [\boldsymbol{p}^c, \boldsymbol{p}^t], \qquad \boldsymbol{S} = [\boldsymbol{S}^c, \boldsymbol{S}^t], \tag{4.5}$$

where quantities with the superscript "c" correspond to the channel elements, while quantities with the superscript "t" refer to the tip elements. This decomposition is essential since the tip widths $\boldsymbol{w}^t$ are determined using the propagation condition (3.1), while the tip pressures $\boldsymbol{p}^t$ are treated as unknowns.

The elasticity equation (2.2) for channel elements can be solved using constant displacement discontinuity (DD) [60] elements to yield

$$\begin{aligned} p^c_{m,n}(t) &= \sigma^{hc}_{m,n} + \sum_{k,l} C_{m-k,n-l} w_{k,l}(t), \\ C_{m-k,n-l} &= -\frac{E'}{8\pi}\left[\frac{\sqrt{(x_m - x)^2 + (y_n - y)^2}}{(x_m - x)(y_n - y)}\right]^{x=x_k+\Delta x/2,\ y=y_l+\Delta y/2}_{x=x_k-\Delta x/2,\ y=y_l-\Delta y/2}, \end{aligned} \tag{4.6}$$

where $p^c_{m,n}$ are the fluid pressure values at the channel element centers and $\sigma^h_{m,n}$ are the corresponding values of the geological stress. The latter Eq. (4.6) can be conveniently written in the following matrix form

$$\boldsymbol{p}^c = \boldsymbol{\sigma}^{hc} + \boldsymbol{C}\boldsymbol{w}, \tag{4.7}$$

where the coefficients of the fully populated matrix $\boldsymbol{C}$ are determined from (4.6).

The source/leak-off term for channel elements is discretized using the midpoint rule

$$S^c_{m,n} = -2C'[\sqrt{t - t_{m,n}} - \sqrt{t - \Delta t - t_{m,n}}] + \frac{\delta_{mm_0,nn_0}}{\Delta x \Delta y} Q(t)\Delta t. \tag{4.8}$$

Here the trigger times $t_{m,n}$ are defined as the time instants at which the fracture front crosses the midpoint of the given element $\mathcal{A}_{m,n}$, and are calculated using interpolation of the front position history. The term δ_{mm_0,nn_0} denotes the Kronecker delta, where the indexes m_0 and n_0 correspond to the element located at the origin where the fluid source is applied.

As follows from (4.4), (4.5), (4.7), and (4.8), the remaining task is to determine $\boldsymbol{w}^t$ and $\boldsymbol{S}^t$, which are both related to the fracture front dynamics and are considered next. Once $\boldsymbol{w}^t$ and $\boldsymbol{S}^t$ are calculated, Eq. (4.4) can be solved for $\boldsymbol{w}^c$ and $\boldsymbol{p}^t$ using either fixed point iteration, Picard iteration, or Newton iteration [34]. Efficient preconditioners for solving this system of equations can be found in [62,63]. Further details of the numerical solution are omitted for brevity and can be found in [22,51].

4.2. Locating the fracture front using the level set algorithm

In order to determine distance to the moving fracture front, we are going to assume that the fracture width follows the asymptotic solution (3.15) from the survey elements to the crack front. In this situation, having determined the

trial fracture widths $\boldsymbol{w}^s$ at the survey elements, the new location of the fracture front s_i corresponding to w_i^s can be calculated using (3.1) by determining the value of s_i that satisfies

$$\frac{s_i^2 V_i \mu'}{E'(w_i^s)^3} = g_\delta\Big(\frac{K' s_i^{1/2}}{E' w_i^s}, \frac{2 s_i^{1/2} C'}{w_i^s V_i^{1/2}}\Big), \qquad V_i = \frac{s_i - s_{i,0}}{\Delta t}, \tag{4.9}$$

where $s_{i,0}$ is the known position of the fracture front at the previous time step and the quantities with the subscript "i" correspond to the ith survey element. Here s_i and $s_{i,0}$ are the distances from the ith survey element to the fracture front at the current and previous time steps respectively. In a situation when the fracture front moves, Eq. (4.9) is solved numerically to determine s_i for the current set of survey elements using Newton's method. If the fracture front does not propagate, then the velocity is zero and hence the fracture front does not move. This is automatically captured by (4.9) since the function g_δ is vanishes for $K' s_i^{1/2}/(E' w_i^s) > 1$, which in turn leads to $V_i = 0$ and $s_i = s_{i,0}$.

To track the fracture front efficiently in the plane, we introduce a signed distance function $\mathcal{T}(x, y)$, which is equal to the negative distance to the fracture front at every point (x, y). In this case, the function $\mathcal{T}$ is a level set function that defines $\mathcal{C}$, since $\mathcal{T}(x, y) < 0$ for all points (x, y) that lie within the fracture boundary curve $\mathcal{C}(t)$, points for which $\mathcal{T}(x, y) > 0$ lie outside $\mathcal{C}(t)$, while the fracture boundary curve $\mathcal{C}(t)$ is defined by the level set $\mathcal{T}(x, y) = 0$. Knowing the distances from all survey elements to the crack front, we can formulate an initial condition for the function $\mathcal{T}$ as

$$\mathcal{T}(x_i, y_i) = -s_i \quad \text{for all } (x_i, y_i) \in \mathcal{A}^s. \tag{4.10}$$

To calculate the values of $\mathcal{T}$ in the narrow band of elements that includes all the tip elements $\mathcal{A}^t$, the Eikonal equation is solved

$$|\nabla \mathcal{T}| = \sqrt{\Big(\frac{\partial \mathcal{T}}{\partial x}\Big)^2 + \Big(\frac{\partial \mathcal{T}}{\partial y}\Big)^2} = 1. \tag{4.11}$$

A simple first order scheme [64,65] to discretize the Eikonal equation (4.11) is used. To illustrate the procedure for calculating the $\mathcal{T}$ function, the right panel in Fig. 3 shows the schematics for calculating the value of $\mathcal{T}_3$ knowing the values $\mathcal{T}_1$ and $\mathcal{T}_2$ in the neighboring elements. The value of $\mathcal{T}_3$ can be calculated either via a first-order discretization of (4.11) or by geometric considerations [22] using the formula

$$\mathcal{T}_3 = \frac{\mathcal{T}_1 + \beta \mathcal{T}_2 + \Theta}{1 + \beta^2}, \tag{4.12}$$

where $\Theta = \sqrt{\Delta x^2 (1 + \beta^2) - \beta^2 \Delta \mathcal{T}^2}$, $\beta = \Delta x / \Delta y$, and $\Delta \mathcal{T} = \mathcal{T}_2 - \mathcal{T}_1$. The fast marching method [64] is then used to extend the initial values of $\mathcal{T}$ (4.10) to a narrow band that includes the fracture front. Knowing the $\mathcal{T}$ values in the tip elements, the location and orientation of the fracture front are defined by [22]

$$\ell = -\frac{\mathcal{T}_1 + \mathcal{T}_2}{2}, \qquad \tan\alpha = \frac{\beta(\Theta - \Delta \mathcal{T})}{\Theta + \beta^2 \Delta \mathcal{T}}, \tag{4.13}$$

where ℓ is the distance from the front to the farthest interior corner of a tip element and α is the inclination of the fracture front (see Fig. 3). Finally, the normal velocity field of the fracture front in the tip elements can be determined using

$$V_j = \frac{\mathcal{T}(x_j, y_j, t - \Delta t) - \mathcal{T}(x_j, y_j, t)}{\Delta t}, \qquad (x_j, y_j) \in \mathcal{A}^t. \tag{4.14}$$

It should be noted here that the velocities V_j can be different from the velocities that are associated with the motion of the front calculated in (4.9).

4.3. Tip volume calculation

Since the displacement discontinuity method assigns the width field in partially filled tip elements $\boldsymbol{w}^t$ to be the average volume of fluid contained in those elements, it is necessary to determine the fluid volume in the tip elements. Once the current location ℓ, orientation α, and normal front speed V are calculated for some tip element using the

level set scheme described above (here a general tip element is considered, in which case the index is omitted), the fluid volume corresponding to the tip asymptote can be calculated [22]. As can be seen from the right panel in Fig. 3, the fluid occupies the polygonal region $ADEFG$. The fluid volume in $ADEFG$ can be calculated as

$$\mathcal{V}_{ADEFG} = \mathcal{V}_{ABC} - \mathcal{H}(\ell - \Delta y \sin\alpha)\mathcal{V}_{GFC} - \mathcal{H}(\ell - \Delta x \cos\alpha)\mathcal{V}_{DBE}, \tag{4.15}$$

where $\mathcal{V}_{ABC}$ is the volume of fluid inside the triangle ABC (note that G and F disappear when $\ell < \Delta y \sin\alpha$, likewise D and E disappear when $\ell < \Delta x \cos\alpha$), $\mathcal{V}_{GFC}$ is the fluid volume inside the triangle GFC (which is accounted for as soon as the triangle GFC exists), $\mathcal{V}_{DBE}$ is the fluid volume inside the triangle DBE (which is accounted for as soon as the triangle DBE exists), and $\mathcal{H}$ denotes the Heaviside step function. Therefore, it is sufficient to calculate the fluid volume associated with the asymptote w_a over a triangular region. To this end, the fluid volume for the asymptotic solution within the triangle ABC can be calculated as

$$\begin{aligned}\mathcal{V}_{ABC} &= \frac{1}{\sin\alpha\cos\alpha}\int_0^\ell s\, w_a(\ell - s)\, ds = \frac{1}{\sin\alpha\cos\alpha}\int_0^\ell (\ell - \xi) w_a(\xi)\, d\xi \\ &= \frac{\ell M_0(\ell) - M_1(\ell)}{\sin\alpha\cos\alpha} \equiv \mathcal{V}_{\triangle}(\ell),\end{aligned} \tag{4.16}$$

where the moments M_0 and M_1 are calculated using (3.18). By using the definition of $\mathcal{V}_{\triangle}(\ell)$ in (4.16) and calculating the volumes of the triangles GFC and DBE similarly to (4.16), Eq. (4.15) can be rewritten as

$$\mathcal{V}_{ADEFG} = \mathcal{V}_{\triangle}(\ell) - \mathcal{H}(\ell - \Delta y \sin\alpha)\mathcal{V}_{\triangle}(\ell - \Delta y \sin\alpha) - \mathcal{H}(\ell - \Delta x \cos\alpha)\mathcal{V}_{\triangle}(\ell - \Delta x \cos\alpha). \tag{4.17}$$

Since the function $\mathcal{V}(\ell)$ is not defined for $\alpha = 0$ and $\alpha = \pi/2$, these two cases have to be considered separately and lead to $\mathcal{V}_{ADEFG} = \Delta y M_0(\ell)$ and $\mathcal{V}_{ADEFG} = \Delta x M_0(\ell)$ respectively. Finally, the average fracture aperture in the jth tip element w_j^t is calculated as

$$w_j^t = \frac{1}{\Delta x \Delta y}\begin{cases} \mathcal{V}_{\triangle}(\ell) - \mathcal{H}(\ell - \Delta y \sin\alpha)\mathcal{V}_{\triangle}(\ell - \Delta y \sin\alpha) & \\ \quad - \mathcal{H}(\ell - \Delta x \cos\alpha)\mathcal{V}_{\triangle}(\ell - \Delta x \cos\alpha), & \alpha \neq 0,\ \alpha \neq \dfrac{\pi}{2}, \\ \Delta y M_0(\ell), & \alpha = 0, \\ \Delta x M_0(\ell), & \alpha = \dfrac{\pi}{2}, \end{cases} \tag{4.18}$$

where ℓ and α correspond to the distance to the front and its orientation (see the right picture in Fig. 3) in the jth tip element. The collection of all w_j^t allows us to obtain $\boldsymbol{w}^t$. Also note that the tip volume (4.18) implicitly depends on the front velocity V since the fracture width asymptotic solution $w_a(\ell)$ depends on the velocity, the moments $M_0(\ell)$ and $M_1(\ell)$ depend on $w_a(\ell)$, and $\mathcal{V}_{\triangle}(\ell)$ in (4.16) depends on the moments.

In situations when the front moves, i.e. $V > 0$, Eq. (3.15) allows us to find $w_a(\ell)$, and eventually calculate tip volumes using (4.18). The case $V = 0$ needs to be considered separately since $w_a(\ell)$ can be calculated using (3.15) only after the stress intensity factor is computed. To determine the latter stress intensity factor, let us consider the situation shown on the right panel in Fig. 3. Since $V = 0$, then according to (3.15) the tip solution is $w_a = K_I' s^{1/2}/E'$. By denoting the width in the survey elements by w_1^s and w_2^s and the corresponding distances to the front $s_1 = -\mathcal{T}_1$ and $s_2 = -\mathcal{T}_2$, the scaled downstream stress intensity factor can be computed using least-squares as

$$K_I' = E' \frac{w_1^s s_1^{1/2} + w_2^s s_2^{1/2}}{s_1 + s_2}. \tag{4.19}$$

Once the stress intensity factor is obtained, the fracture width $w_a(\ell)$ is calculated using the second equation in (3.15) and (4.19). Then the moments are calculated using (3.18), and, finally, the fracture widths in the tip elements with zero velocity are calculated using (4.16) and (4.18).

4.4. Leak-off from the tip elements

To calculate the leak-off volume in the tip elements $\mathbf{S}^t$, we again make reference to the right panel in Fig. 3, in which a typical tip element is shown. To simplify calculations, it is assumed that the time history of the front velocity

$V(t) = d\ell(t)/dt$ is known and that the front orientation does not change, i.e. $\alpha(t) = \alpha$. Similar to the analysis in Section 4.3, firstly, the leak-off from the triangular area ABC (see Fig. 3) is considered. As follows from (2.5) and (4.2), the leak-off volume from the triangular region ABC is determined by the following integral:

$$\begin{aligned}\mathcal{L}_{ABC} &= -\frac{2C'}{\sin\alpha\cos\alpha}\int_0^{\ell}\sqrt{t-t_0(s)}\,s\,ds = -\frac{C'}{\sin\alpha\cos\alpha}\int_0^{\sqrt{t-t_A}}\Big[\int_0^{t-t_A-\zeta^2} V(t'+t_A)\,dt'\Big]^2 d\zeta \\ &\equiv \mathcal{L}_{\triangle}(t,t_A),\end{aligned} \tag{4.20}$$

which is obtained using integration by parts and the variable change $\zeta = \sqrt{t-t_0(s)}$, and where t_A is time at which the fracture front enters the element at point A. Note that $\mathcal{L}_{\triangle}(t,t_A)$ signifies total leak-off from the triangular region ABC during the time period from t_A to t. In the situation when $V = \text{const.}$, Eq. (4.20) reduces to

$$\mathcal{L}_{\triangle}(t,t_A) = -\frac{8}{15}\frac{C'V^2(t-t_A)^{5/2}}{\sin\alpha\cos\alpha}, \qquad V = \text{const.}, \tag{4.21}$$

which provides a quick estimate for the leak-off if the velocity is constant. Since the fractured area becomes rectangular for $\alpha = 0$ or $\alpha = \pi/2$ and (4.20) is not valid, the leak-off from the tip element is given by to the following integral:

$$\mathcal{L}_{\square}(t,t_A) = -2C'\int_0^{\ell}\sqrt{t-t_0(s)}\,ds = -2C'\int_0^{\sqrt{t-t_A}}\Big[\int_0^{t-t_A-\zeta^2} V(t'+t_A)\,dt'\Big]d\zeta, \tag{4.22}$$

which for $V = \text{const.}$ reduces to

$$\mathcal{L}_{\square}(t,t_A) = -\frac{4}{3}C'V\big(t-t_A\big)^{3/2}, \qquad V = \text{const.} \tag{4.23}$$

As for the tip volume calculations (4.15), the leak-off in the polygon $ADEFG$ can be calculated knowing the contribution of the triangles ABC, GFC, and DBE if $\alpha \neq 0$ and $\alpha \neq \pi/2$, or using the result (4.22) if $\alpha = 0$ or $\alpha = \pi/2$. This can be summarized as

$$\mathcal{L}(t) = \begin{cases} \mathcal{L}_{\triangle}(t,t_A) - \mathcal{H}(t-t_G)\mathcal{L}_{\triangle}(t,t_G) - \mathcal{H}(t-t_D)\mathcal{L}_{\triangle}(t,t_D), & \alpha \neq 0,\ \alpha \neq \dfrac{\pi}{2}, \\ \Delta y\,\mathcal{L}_{\square}(t,t_A), & \alpha = 0, \\ \Delta x\,\mathcal{L}_{\square}(t,t_A), & \alpha = \dfrac{\pi}{2}, \end{cases} \tag{4.24}$$

where the times t_G and t_D are the time instants at which the fracture front was located at G and D respectively, and are implicitly defined through the relations $\ell(t_G) = \Delta y\sin\alpha$ and $\ell(t_D) = \Delta x\cos\alpha$. Finally, since the leak-off term in (2.5) is integrated in time from $t-\Delta t$ to t for a given tip element in the discretized equations (4.4), the leak-off term for the jth tip element can be calculated as

$$S_j^t = \frac{1}{\Delta x\,\Delta y}\big(\mathcal{L}(t) - \mathcal{L}(t-\Delta t)\big). \tag{4.25}$$

The collection of S_j^t, calculated using (4.20)–(4.25) for all tip elements allows us to obtain $\mathbf{S}^t$. For the purpose of having an efficient numerical implementation, a switch between (4.20) and (4.21), as well as (4.22) and (4.23) is implemented based on the velocity history $V(t)$. For example, if $|V(t) - V(t_A)|/V(t_A) > 0.2$ (i.e. when the velocity varies substantially within the element) then the scheme uses (4.20) and (4.22) instead of (4.21) and (4.23).

4.5. Outline of the numerical scheme

In order to better understand the structure of the algorithm, it is useful to briefly describe the primary components of the whole numerical scheme. In order to advance the fracture from time $t-\Delta t$ to t, the system of nonlinear algebraic equations is solved iteratively. At each iteration, the following steps are performed:

- Solve (4.4) and (4.5) for $\boldsymbol{w}^c$ and $\boldsymbol{p}^t$. The footprint location, $\boldsymbol{w}^t$, and $\boldsymbol{S}^t$ are taken from the previous iteration (from the previous time step for the first iteration).

- Calculate distance to the new fracture front from each survey element using (4.9) and the updated widths within the survey elements $\boldsymbol{w}^s$.
- Solve the Eikonal equation (4.11) knowing the updated distances from the survey elements to the fracture front. Determine distance to the front ℓ, front orientation α, and front velocity V for each tip element.
- Calculate tip widths $\boldsymbol{w}^t$ and leak-off $\boldsymbol{S}^t$ using (4.18) and (4.25) respectively, where the latter two equations utilize the values of ℓ, α, and V obtained in the previous step.
- Check convergence. Move to next time step if converged or repeat the iteration loop if not.

Adaptive time stepping is used, in which the time step is reduced if the convergence is not reached after a certain number of iterations.

5. Numerical results

5.1. Radial solution

In order to validate the numerical algorithm ILSA described in Section 4, we first consider the case of a radial fracture (i.e. an axisymmetric crack geometry), which occurs in situations when the fracture diameter is smaller than H, or when $\sigma_1^h = \sigma_2^h = \sigma_3^h$, see Fig. 1. This section compares the ILSA predictions with the numerical solution for a radial hydraulic fracture [52], that utilizes a similar mathematical model, axisymmetry, and also uses the universal asymptotic solution for the tip element. The latter universal asymptote, however, is obtained by interpolation of the numerically calculated solution for a semi-infinite fracture. The Explicit Moving Mesh Algorithm (EMMA) was used to generate the results for a radial fracture, where the latter algorithm is described in [52].

As follows from [52], the solution can be written in dimensionless form as

$$\Omega(\rho,\tau) = \frac{w}{\varepsilon L}, \qquad \Pi(\rho,\tau) = \frac{p}{\varepsilon E'}, \qquad \gamma(\tau) = \frac{R}{L}, \tag{5.1}$$

where Ω is the normalized fracture opening, Π is the scaled fluid pressure, γ is the normalized fracture radius (R is the fracture radius), while $0 \leqslant \rho \leqslant 1$ is the scaled radial coordinate and $\tau = t/t_{mk}$ is the scaled time. The length scale L and the parameter ε that appear in (5.1) are expressed in terms of the problem parameters as

$$\varepsilon = \Big(\frac{\mu'}{E' t_{mk}}\Big)^{1/3}, \qquad L = \Big(\frac{Q_0^3 E' t_{mk}^4}{\mu'}\Big)^{1/9}, \qquad t_{mk} = \Big(\frac{\mu'^5 E'^{13} Q_0^3}{K'^{18}}\Big)^{1/2}. \tag{5.2}$$

All the results depend on a single dimensionless parameter (apart from time) that represents the strength of the leak-off, and can be written as

$$\phi = \frac{\mu'^3 E'^{11} C'^4 Q_0}{K'^{14}}. \tag{5.3}$$

The EMMA algorithm provides the solution in the form of $\Omega(\rho,\tau)$, $\Pi(\rho,\tau)$, and $\gamma(\tau)$ for a given value of ϕ, while the dimensional quantities can be restored via (5.1)–(5.3).

In order to compare the ILSA predictions to the EMMA solution, we set $\mu' = E' = K' = Q_0 = 1$, and, as follows from (5.3), $C' = \phi^{1/4}$, which applies to the rest of this section. In this situation, all the scaling quantities that appear in (5.2) are equal to unity, in which case the scaled (EMMA) and unscaled (ILSA) solutions can be compared directly.

In addition to comparing the length, fracture width, and fluid pressure, it is useful to compare the efficiencies. Efficiency is defined here as the ratio between the fracture volume, and the total fluid volume pumped into the fracture. For ILSA, the efficiency can be calculated as

$$\eta(t) = \frac{1}{Q_0 t} \int_{\mathcal{A}(t)} w(x,y,t)\, dxdy, \tag{5.4}$$

while for EMMA, the efficiency is

$$\eta(t) = \frac{2\pi\gamma^2}{\tau} \int_0^1 \Omega(\rho,\tau)\, \rho d\rho. \tag{5.5}$$

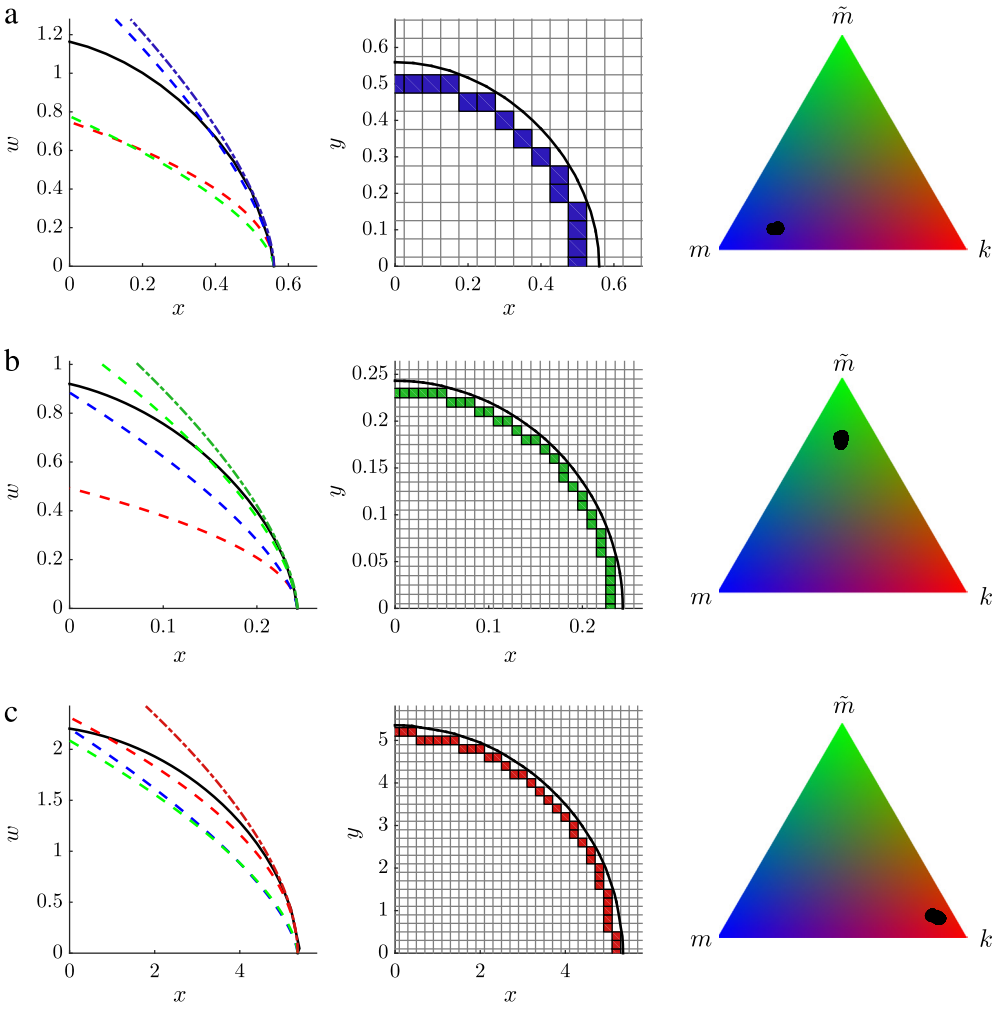

Fig. 4. ILSA results for an axisymmetric hydraulic fracture geometry plotted for: (a) $\phi = 10^{-6}$ and $\tau = 0.67$, (b) $\phi = 1$ and $\tau = 0.22$, (c) $\phi = 10^{-6}$ and $\tau = 170$. Left picture (for each row) plots the variation of the fracture aperture versus spatial coordinate x (black solid line), the universal asymptotic solution (3.15) (dash–dot line with the color corresponding to the location on the parametric triangle), and the vertex solutions (3.3). The latter vertex solutions are indicated by the dashed red line (the toughness asymptotic solution), dashed blue line (the viscous asymptotic solution), dashed green line (the leak-off asymptotic solution). The middle picture shows one quarter of the fracture footprint, the mesh, and highlights the survey elements that are used to locate the moving fracture front. The color filling of such elements correspond to the location of the asymptotic solutions on the parametric triangle used to locate the front. The right picture shows the parametric triangle with the black points corresponding to all survey elements. (For interpretation of the references to color in this figure legend, the reader is referred to the web version of this article.)

In the absence of leak-off, the efficiency is equal to unity due to the global volume balance. For non-zero leak-off, the efficiency decreases with time and eventually approaches zero.

To illustrate the capabilities of the ILSA scheme, Figs. 4 and 5 show the ILSA results for different values of ϕ at different time instants. The left panel (on all plots) shows the variation of the calculated fracture aperture versus x (solid black line), together with the universal asymptotic solution (3.15) (dash–dot line with the color corresponding to the location on the parametric triangle), and the vertex solutions (3.3) (for which $s = \gamma - x$). The toughness asymptotic solution is shown by the dashed red line, the viscous asymptotic solution is shown by the dashed blue line, while the leak-off asymptotic solution is shown by the dashed green line. The middle picture shows the fracture footprint (solid black line, only one quarter is shown due to symmetry), the mesh, and highlights the survey elements that are used to locate the fracture front. The color filling of these elements corresponds to the location of the corresponding asymptotic solutions inside the parametric triangle. It is important to recall here that the asymptotic solution used

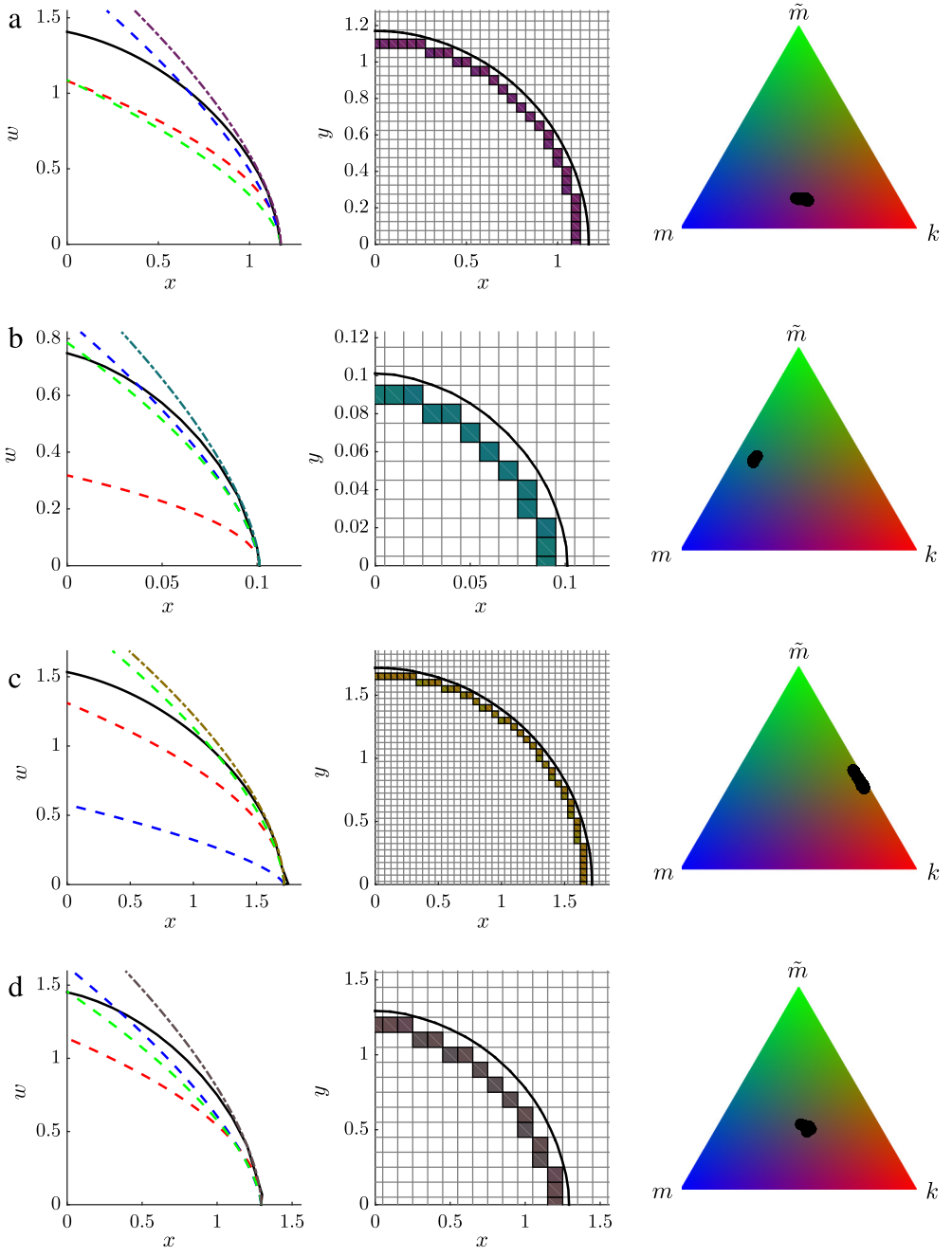

Fig. 5. The same as in Fig. 4, but for: (a) $\phi = 10^{-6}$ and $\tau = 3.8$, (b) $\phi = 1$ and $\tau = 0.019$, (c) $\phi = 1$ and $\tau = 220$, (d) $\phi = 10^{-4}$ and $\tau = 6.1$. (For interpretation of the references to color in this figure legend, the reader is referred to the web version of this article.)

for the survey elements changes with distance. For this reason, different survey elements utilize slightly different asymptotic solutions due to the small difference in the distance to the fracture front, and accordingly have slightly different color filling. The right picture shows the parametric triangle with the black points that correspond to all survey elements. Note that there is a cloud of such points (as opposed to a single point), since the survey elements use slightly different asymptotes to locate the fracture front. Fig. 4(a) plots the ILSA results for $\phi = 10^{-6}$ and $\tau = 0.67$, where the survey elements use a solution that is close to the m vertex. Fig. 4(b) plots the ILSA results for $\phi = 1$ and

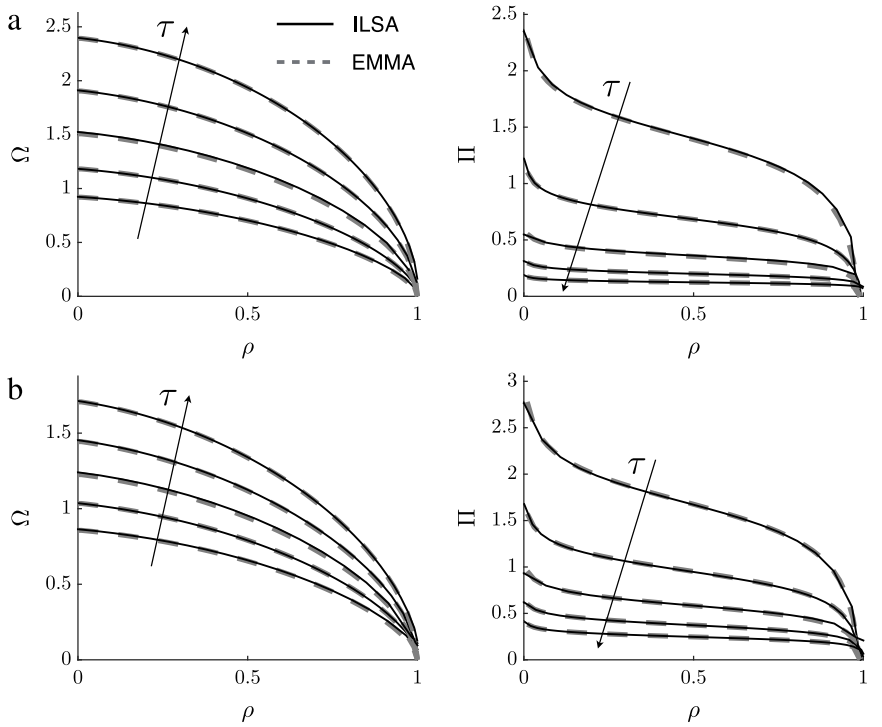

Fig. 6. Comparison between the ILSA (black solid lines) and EMMA (dashed gray lines) numerical solutions in terms of fracture aperture (left) and fluid pressure (right) spatial variations for: (a) $\phi = 10^{-4}$, and (b) $\phi = 1$. The results are shown at the same time instants $\tau = \{10^{-1}, 1, 10, 10^2, 10^3\}$. Arrows schematically indicate the evolution of the solutions with time τ.

$\tau = 0.22$, where the survey elements use a solution that is close to the $\tilde{m}$ vertex. Fig. 4(c) plots the ILSA results for $\phi = 10^{-6}$ and $\tau = 170$, where the survey elements use a solution that is close to the k vertex. Fig. 5(a) plots the ILSA results for $\phi = 10^{-6}$ and $\tau = 3.8$, where the survey elements use a solution that is between the m and k vertices. Fig. 5(b) plots the ILSA results for $\phi = 1$ and $\tau = 0.019$, where survey tip elements use a solution that is between the m and $\tilde{m}$ vertices. Fig. 5(c) plots the ILSA results for $\phi = 1$ and $\tau = 220$, where the survey elements use a solution that is between the k and $\tilde{m}$ vertices. Finally, Fig. 5(d) plots the ILSA results for $\phi = 10^{-4}$ and $\tau = 6.1$, where the survey elements use a solution that is approximately in the middle of the parametric triangle. It is interesting to note that despite the fact that the asymptotic solution is used only for the tip element, the actual region of validity for this solution is larger and spreads over a few elements in the tip region (this depends on the mesh size). For this reason, it is possible to use a relatively coarse mesh together with the asymptotic solution for the tip element to obtain an accurate result. Note that the results shown in Figs. 4 and 5 use $\mu' = E' = K' = Q_0 = 1$, and $C' = \phi^{1/4}$.

To provide a quantitative validation of the ILSA scheme, Fig. 6 compares the fracture opening and fluid pressure profiles inside a radial fracture calculated using ILSA (solid black lines), and the numerical scheme for an axisymmetric fracture EMMA (dashed gray lines) [52] for $\phi = 10^{-4}$ (Fig. 6(a)), and for $\phi = 1$ (Fig. 6(b)) at the same time instants $\tau = \{10^{-1}, 1, 10, 10^2, 10^3\}$. Note here that since ILSA utilizes $\mu' = E' = K' = Q_0 = 1$, the fracture aperture calculated by ILSA is equal to Ω, the fluid pressure is equal to Π (see (5.1) and (5.2)), while ρ is simply the x coordinate that is normalized by the fracture half-length in the x direction. One can clearly see from the results, that both numerical approaches provide nearly identical results, which validates the ILSA method for the case of a radial fracture. The values of $\phi = 10^{-4}$ and $\phi = 1$ are chosen so that the asymptotic solution for the survey elements pass through the middle of the triangle for the case of $\phi = 10^{-4}$, and almost reaches the $\tilde{m}$ vertex for $\phi = 1$, see Figs. 4 and 5.

To provide a further comparison between the ILSA and EMMA solutions, Fig. 7 plots the time histories of the fracture radius and efficiency for different values of the leak-off parameter $\phi = \{10^{-6}, 10^{-4}, 10^{-2}, 1, 10^2, 10^4\}$. The EMMA scheme uses a moving mesh, in which case the algorithm is able to capture the fracture whose length varies

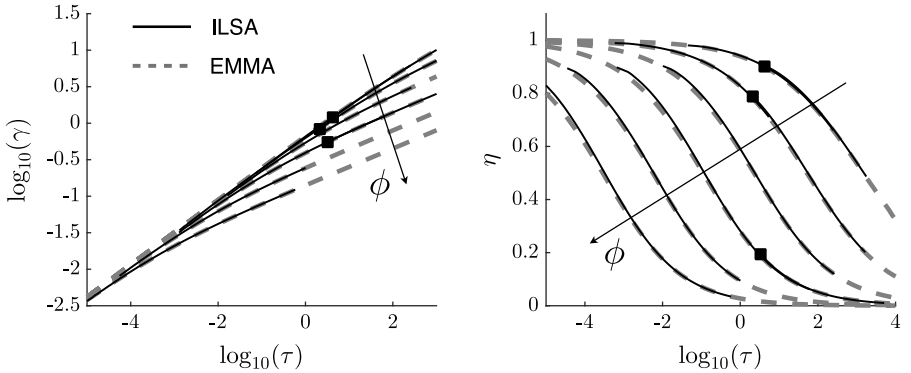

Fig. 7. Comparison between the ILSA and EMMA numerical solutions for an axisymmetric hydraulic fracture in terms of radius and efficiency time histories for $\phi = \{10^{-6}, 10^{-4}, 10^{-2}, 1, 10^{2}, 10^{4}\}$. Arrows schematically indicate the solutions that correspond to different values of ϕ. Black markers show the time instants, at which the ILSA algorithm was restarted on a coarser mesh.

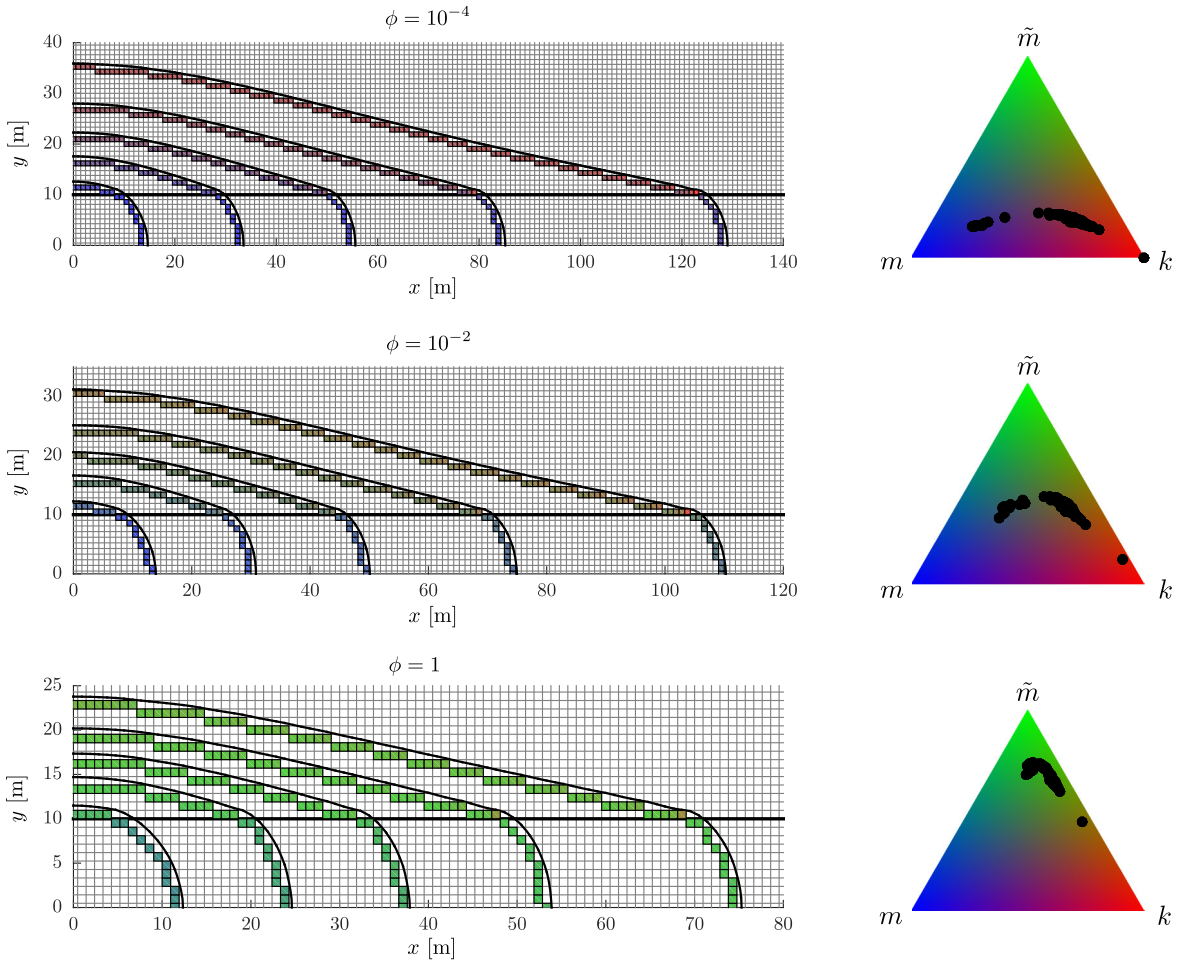

Fig. 8. Hydraulic fracture footprints calculated for the symmetric stress barrier geometry (5.6)–(5.8) for $\phi = 10^{-4}$ (top picture), $\phi = 10^{-2}$ (middle picture), and $\phi = 1$ (bottom picture) at the time instants $t = \{100, 400, 900, 1800, 3600\}$ s. Survey elements are colored according to the location of the corresponding asymptotic solution in the parametric triangle. Black circular markers inside the parametric triangles show positions of all survey elements for the footprint that corresponds to the last time instant $t = 3600$ s. (For interpretation of the references to color in this figure legend, the reader is referred to the web version of this article.)

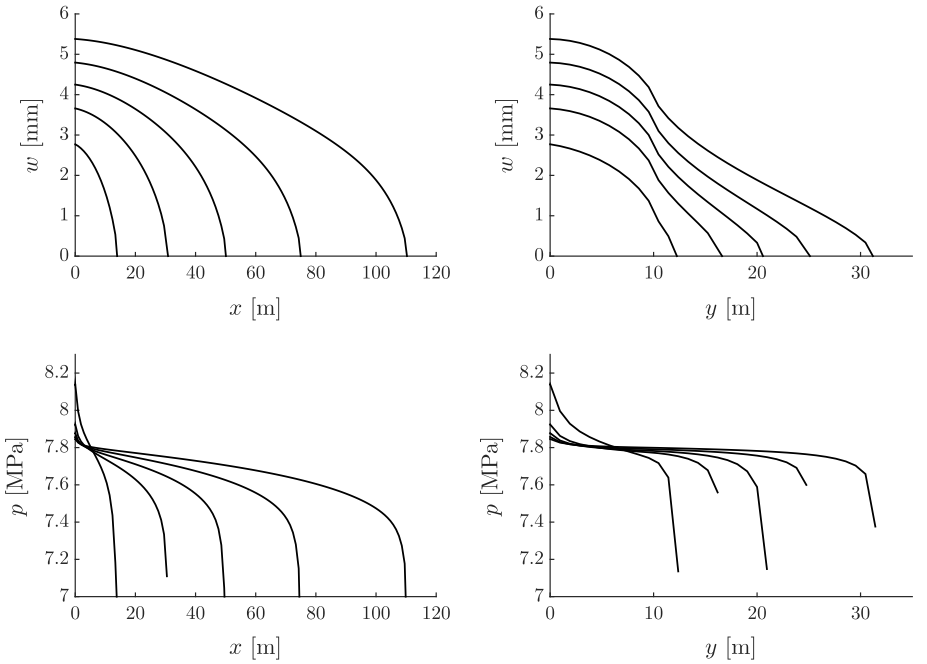

Fig. 9. Variation of fracture width, w, and fluid pressure, p, versus x at $y = 0$ (left pictures) and versus y at $x = 0$ (right pictures) calculated for the symmetric stress barrier geometry (5.6)–(5.8) and $\phi = 10^{-2}$, plotted at $t = \{100, 400, 900, 1800, 3600\}$ s.

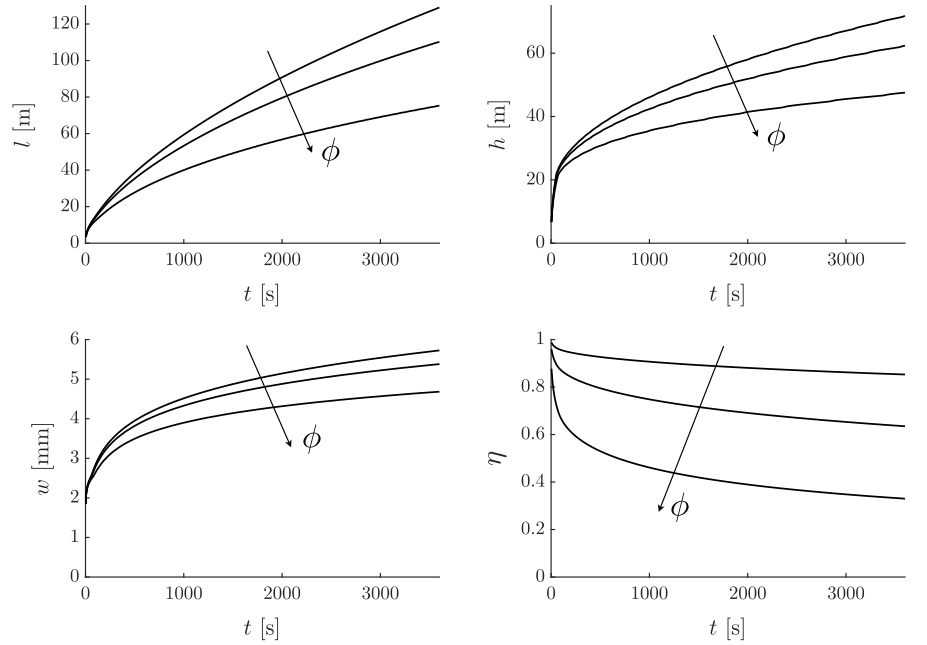

Fig. 10. Time histories of fracture half-length (top left), height (top right), width at the wellbore (bottom left), and efficiency (bottom right) calculated for the symmetric stress barrier geometry (5.6)–(5.8) and $\phi = \{10^{-4}, 10^{-2}, 1\}$. Arrows schematically indicate the direction in which results shift as the parameter ϕ increases.

over a span of multiple orders of magnitude. This is not the case with the ILSA method, in which a fixed mesh is used, and large fractures require significantly more elements, which increases the computational costs. To address the problem, and to obtain ILSA results for large fractures, the numerical code was restarted on a coarser mesh.

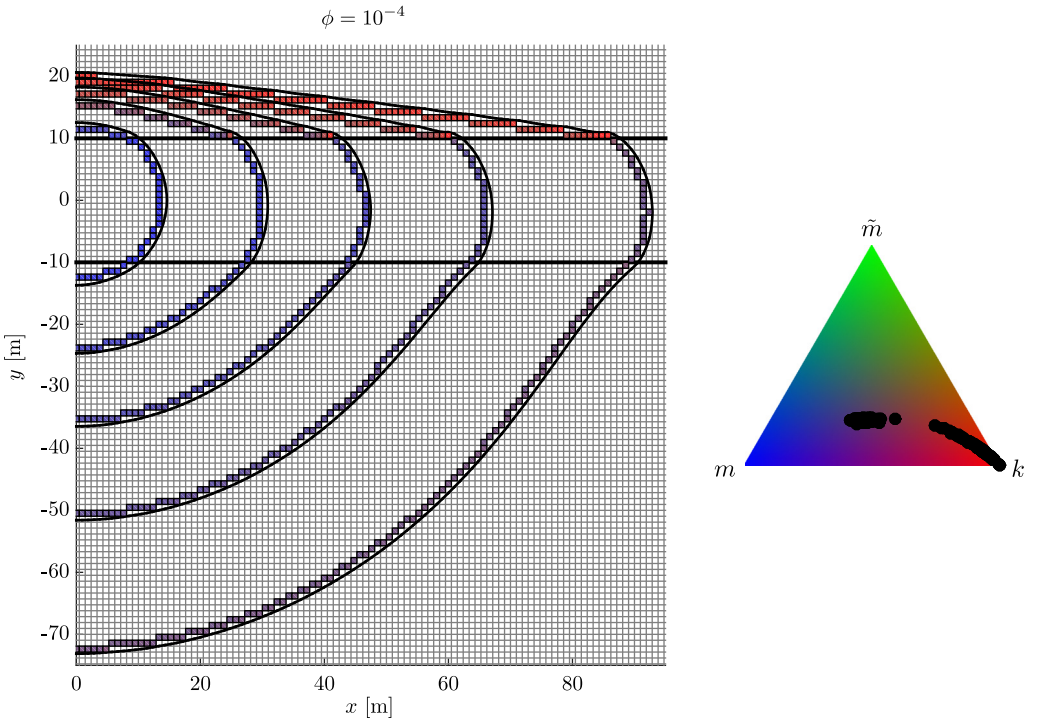

Fig. 11. Hydraulic fracture footprints calculated for the asymmetric stress barrier geometry (5.6), (5.7), and (5.9) for $\phi = 10^{-4}$ at the time instants $t = \{100, 400, 900, 1800, 3600\}$ s. Survey elements are colored according to the location of the corresponding asymptotic solution in the parametric triangle. Black circular markers inside the parametric triangles show positions of all survey elements for the footprint that corresponds to the last time instant $t = 3600$ s. (For interpretation of the references to color in this figure legend, the reader is referred to the web version of this article.)

Interpolation from the finer mesh to the coarser mesh was used to set up an initial condition. Time instants, at which the ILSA code was restarted on a coarser mesh are indicated by the black markers in Fig. 7.

5.2. Planar hydraulic fracture in three stress layers

Having validated the numerical algorithm ILSA for the axisymmetric case in Section 5.1, this section aims to apply it to determine the fracture geometry in situations when the compressive stress varies in a three layer geometry, see Fig. 1. To this end, it is convenient to specify common problem parameters that are used for calculations as

$$E = 9.5 \text{ GPa}, \quad \nu = 0.2, \quad \mu = 0.1 \text{ Pa s}, \quad Q_0 = 0.01 \text{ m}^3/\text{s}, \quad K_{Ic} = 1 \text{ MPa m}^{1/2}, \quad H = 20 \text{ m}. \tag{5.6}$$

Three different values of leak-off are considered, namely

$$C' = \{0.521, 1.65, 5.21\} \times 10^{-5} \text{ m/s}^{1/2} \quad \Longrightarrow \quad \phi = \{10^{-4}, 10^{-2}, 1\}. \tag{5.7}$$

Note that the normalized leak-off parameter ϕ is calculated using the values of material parameters (5.6), scaling (2.1), and the definition of ϕ (5.3). The mesh that is used for all examples is such that $\Delta x = \Delta y = H/21 \approx 0.95$ m. Variable time stepping is employed to ensure stability, and the value of the initial time step is chosen in the range $\Delta t = 1 - 5$ s. Simulations are performed until $t_{\text{end}} = 3600$ s, in which case the number of time steps in each calculation is on the order of 10^3.

5.2.1. Symmetric stress barriers

This section focuses on the case when the central layer is surrounded by two layers with larger but equal compressive stresses (symmetric stress barriers), i.e. $\sigma_1^h = \sigma_3^h > \sigma_2^h$. Values of the compressive stresses in all layers

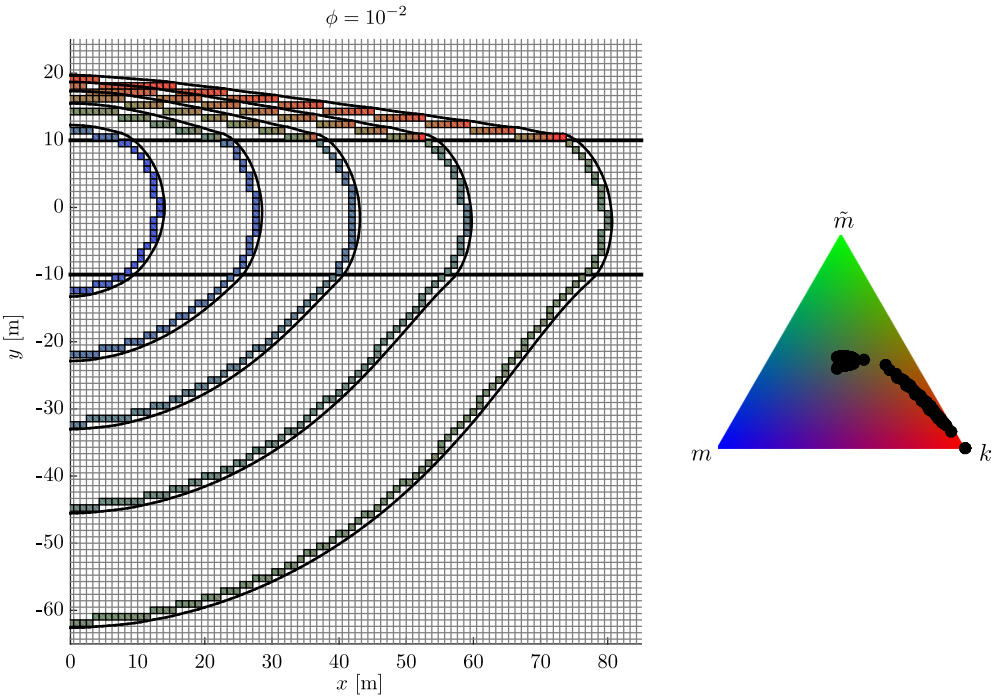

Fig. 12. Hydraulic fracture footprints calculated for the asymmetric stress barrier geometry (5.6), (5.7), and (5.9) for $\phi = 10^{-2}$ at the time instants $t = \{100, 400, 900, 1800, 3600\}$ s. Survey elements are colored according to the location of the corresponding asymptotic solution in the parametric triangle. Black circular markers inside the parametric triangles show positions of all survey elements for the footprint that corresponds to the last time instant $t = 3600$ s. (For interpretation of the references to color in this figure legend, the reader is referred to the web version of this article.)

are prescribed as follows:

$$\sigma_1^h = 7.75 \text{ MPa}, \qquad \sigma_2^h = 7 \text{ MPa}, \qquad \sigma_3^h = 7.75 \text{ MPa}. \tag{5.8}$$

Figs. 8–10 plot the results of the numerical calculations for the parameters (5.6), (5.7), and (5.8).

Fig. 8 shows the fracture footprints that are calculated for three different values of leak-off $\phi = \{10^{-4}, 10^{-2}, 1\}$ and are plotted at $t = \{100, 400, 900, 1800, 3600\}$ s. Thick solid black lines indicate the boundaries between adjacent geological layers. Survey elements are colored according to the asymptotic solution that is used to locate the fracture front. This coloring procedure, as well as the properties of the parametric triangle are described in Section 3.4. Black circular markers inside the parametric triangles indicate the locations of all survey elements that correspond to the largest footprint (i.e. the one plotted at $t = 3600$ s). One can clearly observe that the change of the leak-off parameter ϕ causes a substantial change of the asymptotic solution that is used in calculations, and affects the fracture size. In addition, different parts of the same fracture use different solutions due to variation of fracture front velocity, which highlights the importance of using the universal asymptotic solution.

To illustrate the variation of the fracture width and pressure, Fig. 9 shows the variation of the width and pressure along the x axis ($y = 0$) and along the y axis ($x = 0$) at $t = \{100, 400, 900, 1800, 3600\}$ s. Only the case of $\phi = 10^{-2}$ is considered for brevity, since the results for other values of ϕ are qualitatively similar. Since, in this example, the fracture grows monotonically with time, curves that correspond to larger fracture size represent larger times. It is interesting to observe effect of the stress barrier on the fracture width variation along the y axis, which suppresses the width after $y > \frac{1}{2}H = 10$ m. Also, the pressure is nearly constant along the y coordinate, which validates the assumption of uniform pressure that is used in pseudo-3D models [66,19].

Fig. 10 plots the time histories of the fracture half-length, height, width at the wellbore ($x = y = 0$), and efficiency for different values of leak-off $\phi = \{10^{-4}, 10^{-2}, 1\}$ for the symmetric stress barrier case. Here the fracture half-length is calculated as the fracture extension along the x axis, i.e. at $y = 0$, while the fracture height is determined at $x = 0$. As for the radial fracture, the efficiency is defined as the ratio between fracture volume and the total pumped fluid

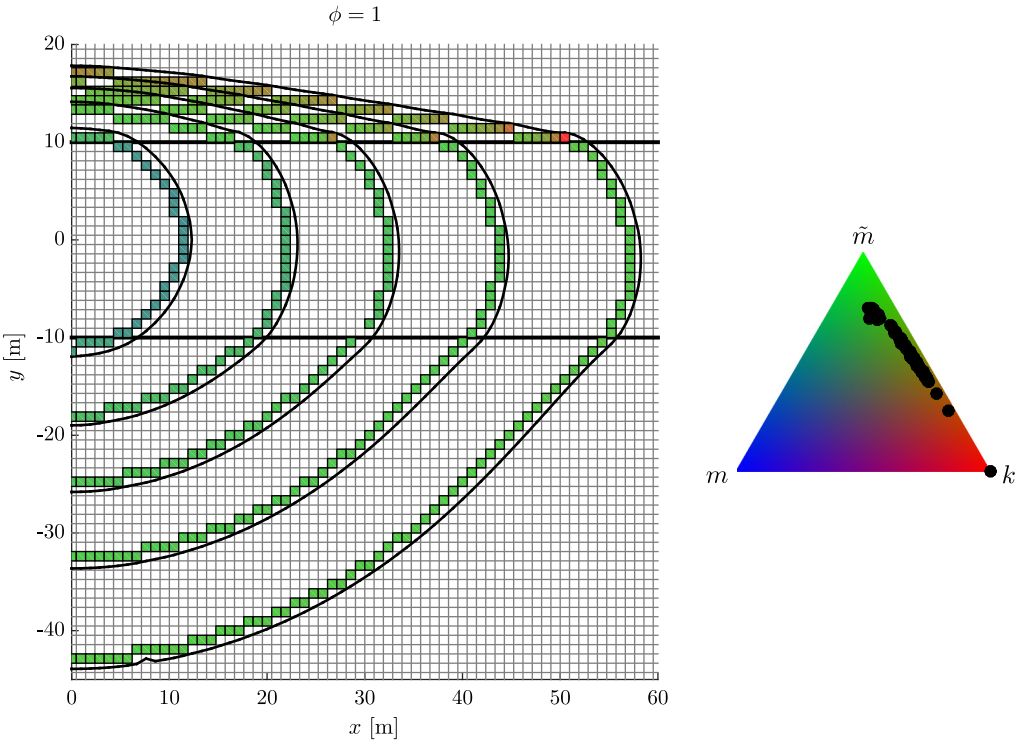

Fig. 13. Hydraulic fracture footprints calculated for the asymmetric stress barrier geometry (5.6), (5.7), and (5.9) for $\phi = 1$ at the time instants $t = \{100, 400, 900, 1800, 3600\}$ s. Survey elements are colored according to the location of the corresponding asymptotic solution in the parametric triangle. Black circular markers inside the parametric triangles show positions of all survey elements for the footprint that corresponds to the last time instant $t = 3600$ s. (For interpretation of the references to color in this figure legend, the reader is referred to the web version of this article.)

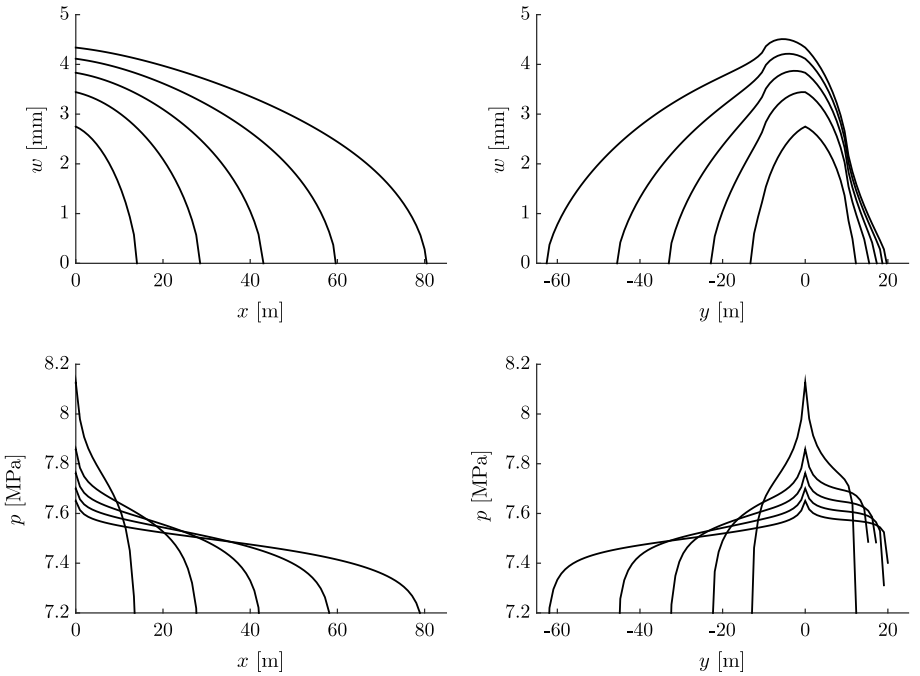

Fig. 14. Variation of fracture width, w, and fluid pressure, p, versus x at $y = 0$ (left pictures) and versus y at $x = 0$ (right pictures) calculated for asymmetric stress barrier geometry (5.6), (5.7), (5.9) and $\phi = 10^{-2}$, plotted at $t = \{100, 400, 900, 1800, 3600\}$ s.

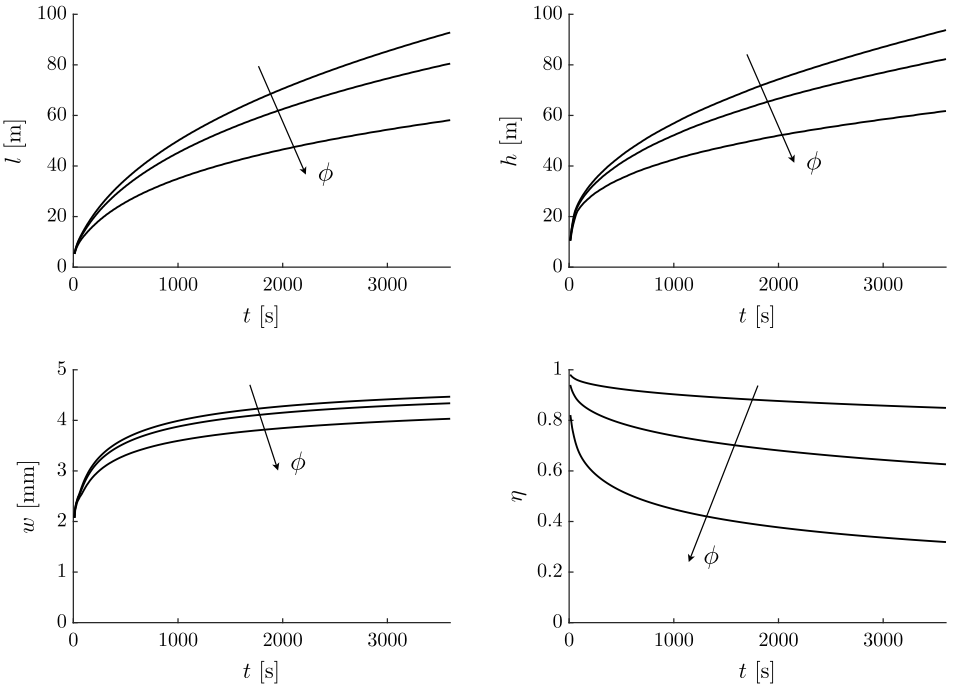

Fig. 15. Time histories of fracture half-length (top left), height (top right), width at the wellbore (bottom left), and efficiency (bottom right) calculated for asymmetric stress barrier geometry (5.6), (5.7), (5.9) and $\phi = \{10^{-4}, 10^{-2}, 1\}$. Arrows schematically indicate the direction in which results shift as the parameter ϕ increases.

volume (5.4). An increase in leak-off reduces the fracture length and height, which is consistent with the results shown in Fig. 8. The fracture aperture and efficiency also become smaller.

5.2.2. *Asymmetric stress barriers*

A problem with asymmetric stress barriers, for which $\sigma_3^h > \sigma_1^h > \sigma_2^h$, is examined next. In particular, the simulations are performed for the parameters (5.6), (5.7), and the following values of compressive stresses:

$$\sigma_1^h = 7.25 \text{ MPa}, \qquad \sigma_2^h = 7 \text{ MPa}, \qquad \sigma_3^h = 7.75 \text{ MPa}. \tag{5.9}$$

Figs. 11–15 plot results of the numerical calculations.

Similar to Fig. 8, Figs. 11–13 plot fracture footprints at $t = \{100, 400, 900, 1800, 3600\}$ s for three different values of the leak-off parameter $\phi = \{10^{-4}, 10^{-2}, 1\}$. The primary difference is the smaller value of the stress barrier for the bottom layer, which makes it easier for the fracture to grow downwards. This, in turn, slows the propagation through the upper layer, in which case the asymptotic solutions that are used to calculate fracture growth are closer to the "k" vertex (asymptotic solution exactly corresponds to the "k" vertex for zero velocity).

Fig. 14 plots the variation of fracture width and pressure versus x at $y = 0$ and versus y at $x = 0$ for the asymmetric stress barrier case for $\phi = 10^{-2}$. This figure is an analog of Fig. 9. The most significant difference occurs in the variation of width and pressure along the y axis. In particular, the fracture is substantially wider within the weaker stress barrier, while the pressure is smaller. The maximum opening is not located at the wellbore, but is shifted towards the weaker stress barrier.

Fig. 15 plots time histories of the fracture half-length, height, width at the wellbore ($x = y = 0$), and efficiency for different values of leak-off $\phi = \{10^{-4}, 10^{-2}, 1\}$ for the asymmetric stress barrier case. As for the symmetric stress barrier case, the fracture half-length is calculated as the fracture extension along the x axis, i.e. at $y = 0$, while the fracture height is determined at $x = 0$. Note, however, that the half-length defined above is slightly smaller than the maximum fracture extension in the horizontal direction, as can be seen from Figs. 11–13. This happens because the smaller stress barrier causes asymmetry of the fracture front in the central layer. As in Fig. 10, larger leak-off results correspond to smaller fracture length and height, wellbore width, and efficiency. Despite the fact that Figs. 10 and 15

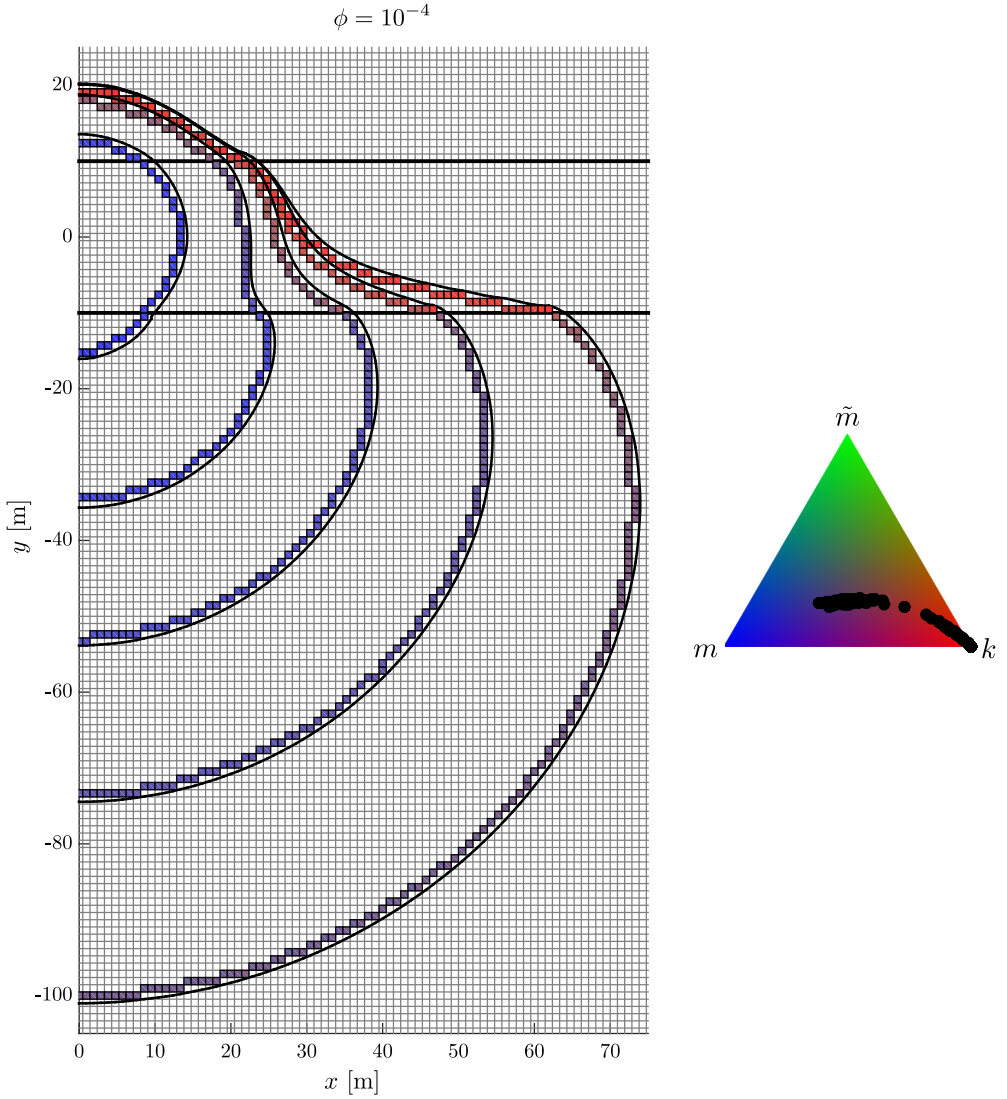

Fig. 16. Hydraulic fracture footprints calculated for the stress drop geometry (5.6), (5.7), and (5.10) for $\phi = 10^{-4}$ at the time instants $t = \{100, 400, 900, 1800, 3600\}$ s. Survey elements are colored according to the location of the corresponding asymptotic solution in the parametric triangle. Black circular markers inside the parametric triangles show positions of all survey elements for the footprint that corresponds to the last time instant $t = 3600$ s. (For interpretation of the references to color in this figure legend, the reader is referred to the web version of this article.)

indicate qualitatively similar behavior for the symmetric and the asymmetric stress barrier cases, there is a noticeable quantitative difference.

5.2.3. *Stress drop problem*

Finally, the problem with a stress drop, for which $\sigma_3^h > \sigma_2^h > \sigma_1^h$, is considered. The calculations are performed for the parameters (5.6), (5.7), and the following values of compressive stresses:

$$\sigma_1^h = 6.5 \text{ MPa}, \qquad \sigma_2^h = 7 \text{ MPa}, \qquad \sigma_3^h = 7.25 \text{ MPa}. \tag{5.10}$$

The results of the numerical calculations are summarized in Figs. 16–20.

Figs. 16–18 show the hydraulic fracture footprints for the stress drop problem at $t = \{100, 400, 900, 1800, 3600\}$ s for three different values of the leak-off parameter $\phi = \{10^{-4}, 10^{-2}, 1\}$. These figures are the analogs of Fig. 8

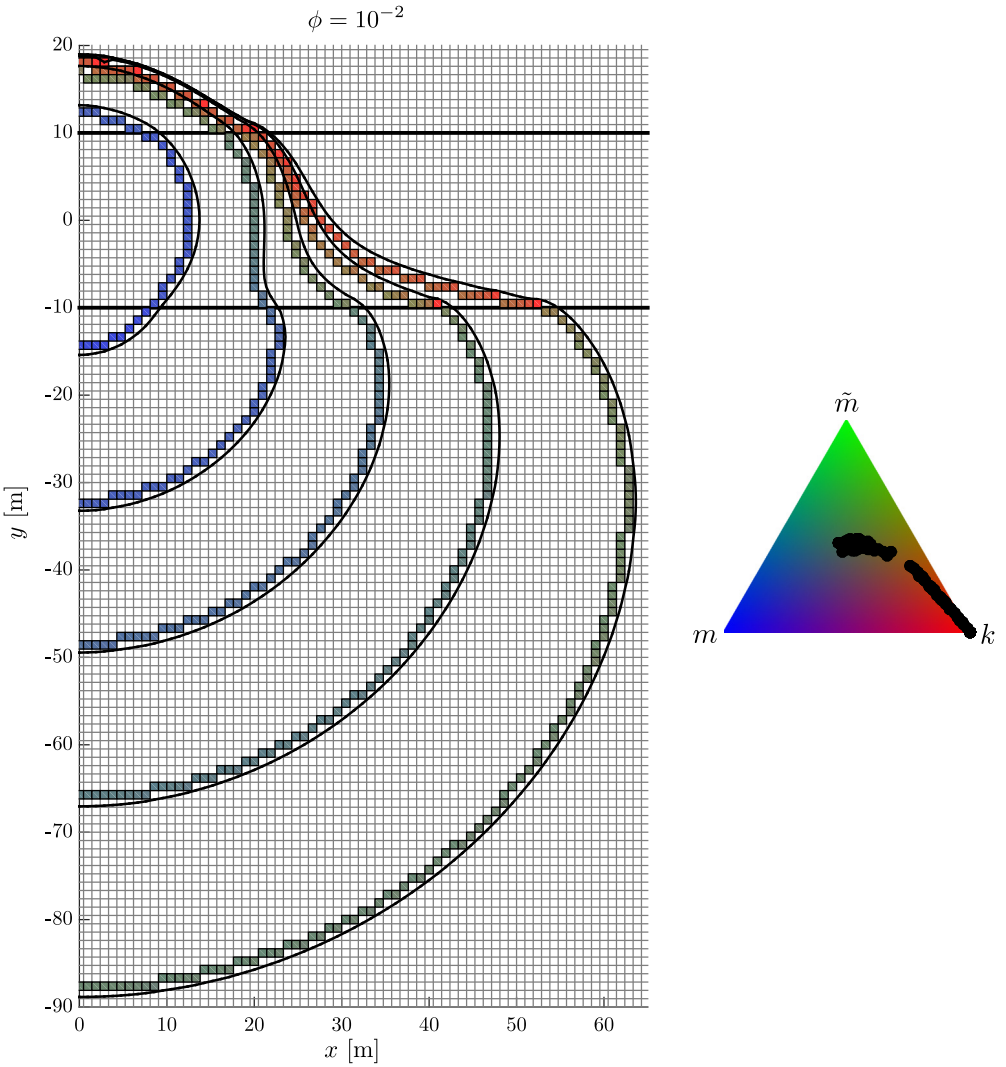

Fig. 17. Hydraulic fracture footprints calculated for the stress drop geometry (5.6), (5.7), and (5.10) for $\phi = 10^{-2}$ at the time instants $t = \{100, 400, 900, 1800, 3600\}$ s. Survey elements are colored according to the location of the corresponding asymptotic solution in the parametric triangle. Black circular markers inside the parametric triangles show positions of all survey elements for the footprint that corresponds to the last time instant $t = 3600$ s. (For interpretation of the references to color in this figure legend, the reader is referred to the web version of this article.)

for the symmetric stress barrier case and Figs. 11–13 for the asymmetric stress barrier case. The presence of a stress drop drives the fracture to propagate mostly downwards and, as a result, the propagation through the top layer is practically arrested after some period of time. In this case, the second equation in (3.15) and (4.19) are used to determine the tip widths for completely immobile regions of the fracture front in the top part of the fracture.

Fig. 19 plots variation of the fracture width and pressure versus x at $y = 0$ for the stress drop case for $\phi = 10^{-2}$. Note here that the variation of fracture aperture and pressure versus x for $y = 0$ is omitted since it is not informative, see Figs. 16–18. Since level of the compressive stress is the smallest in the stress drop region, the fracture width reaches its maximum there (in the stress drop region) for relatively mature fractures. This is also the reason for the very asymmetric height growth, for which the propagation occurs primary in the bottom part of the fracture. The pressure levels are substantially different in the bottom and the top parts of the fracture due to the variation in the compressive stresses. At some point, the top fracture front stops propagating, in which case the characteristic pressure drop near the tip disappears. In the latter case, the pressure in the top part becomes close to the compressive stress

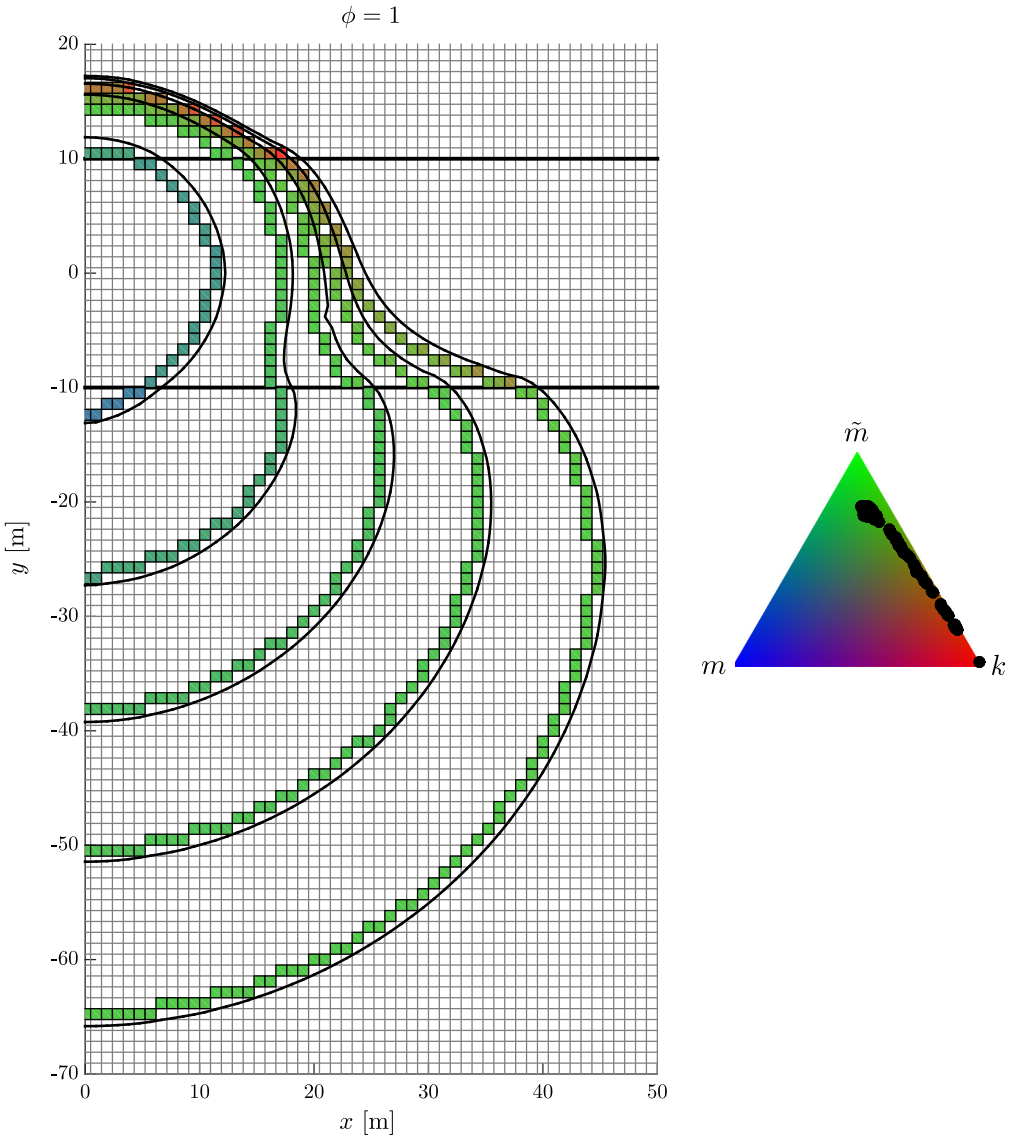

Fig. 18. Hydraulic fracture footprints calculated for the stress drop geometry (5.6), (5.7), and (5.10) for $\phi = 1$ at the time instants $t = \{100, 400, 900, 1800, 3600\}$ s. Survey elements are colored according to the location of the corresponding asymptotic solution in the parametric triangle. Black circular markers inside the parametric triangles show positions of all survey elements for the footprint that corresponds to the last time instant $t = 3600$ s. (For interpretation of the references to color in this figure legend, the reader is referred to the web version of this article.)

value $\sigma_3^h = 7.25$ MPa. Note that the fluid pressure is higher than the compressive stress in the lower part of the fracture due to fracture propagation, which together with the viscous fluid flow requires a pressure gradient.

Fig. 20 plots time histories of the fracture width at the wellbore ($x = y = 0$), and efficiency for different values of leak-off $\phi = \{10^{-4}, 10^{-2}, 1\}$ for the stress drop case. Note that the fracture half-length, defined as the fracture extension at $y = 0$, is not very informative, as can be seen from Figs. 16–18, and therefore is not shown. Due to significant asymmetry, the height growth history is omitted too. At the same time, it is interesting to observe that the fracture width at the wellbore has a maximum, after which it decays to a plateau value. This happens because the fracture growth occurs primarily in the stress drop zone after some time, see Fig. 19. In addition, the wellbore width varies insignificantly with leak-off. Finally, it is interesting to observe that the efficiency plots for the symmetric, asymmetric, and stress drop geometric shown in Figs. 10, 15, and 20 are all very similar despite the drastic change in geometry.

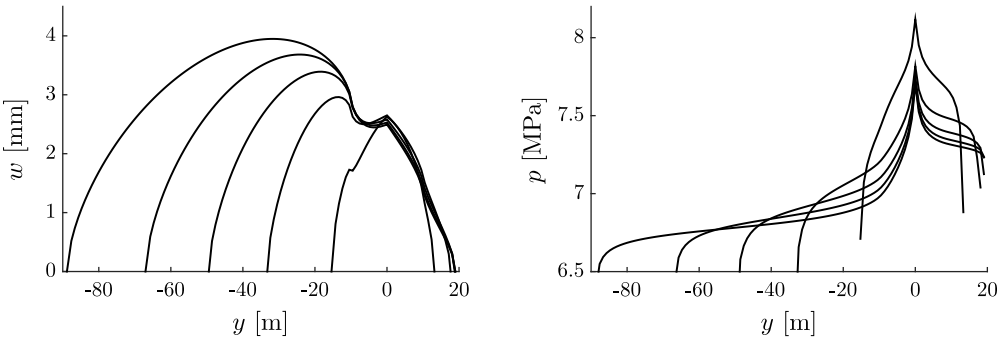

Fig. 19. Variation of the fracture width (left) and the fluid pressure (right) versus x at $y = 0$ calculated for the stress drop geometry (5.6), (5.7), (5.10) and $\phi = 10^{-2}$, plotted at $t = \{100, 400, 900, 1800, 3600\}$ s.

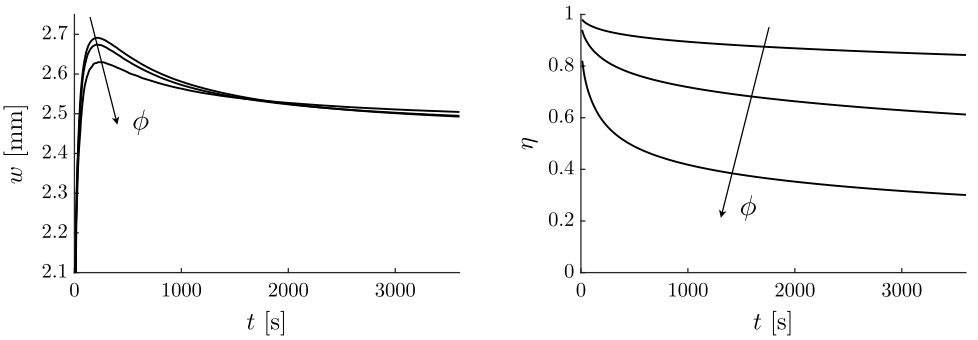

Fig. 20. Time histories of the fracture width at the wellbore (left), and efficiency (right) calculated for stress drop geometry (5.6), (5.7), (5.10) and $\phi = \{10^{-4}, 10^{-2}, 1\}$. Arrows schematically indicate the direction in which results shift as the parameter ϕ increases.

6. Summary

This paper describes an Implicit Level Set Algorithm (ILSA) for modeling planar hydraulic fractures that is able to capture, on a relatively coarse mesh, the multiscale behavior associated with the three competing physical processes of energy release associated with fracture toughness, viscous dissipation due to fluid flow, and fluid leak-off into the surrounding rock. The model captures the fracture propagation dynamics by coupling the solution of the elastic equilibrium equations, the lubrication equation associated with fluid conservation and laminar flow of a Newtonian fluid via Poiseuille's law, and leak-off into the formation via Carter's model, and a propagation condition in which the stress intensity factor at the fracture front is in limit equilibrium with the fracture toughness. The numerical scheme utilizes the displacement discontinuity method for the elasticity calculations, while the finite volume scheme is used for the fluid flow. Incorporating leak-off involves the inclusion of a delay term containing the trigger time history, so that modeling a propagating hydraulic fracture involves solving a fully coupled integro-delay-PDE. Accounting for the leak-off from tip elements, in which the fracture front has experienced significant speed changes, required the development of a specialized integration scheme that involves the front velocity history. The fracture front propagation is tracked using an implicit level set method, which uses a ring of elements that are located inside the fracture and adjacent to the fracture tip to determine the distance to the fracture front assuming that the fracture width in the tip region follows the multiscale tip asymptotic solution. The latter tip asymptotic solution comes from a local asymptotic analysis of the tip region of a hydraulic fracture, which reduces to the problem of a steadily propagating semi-infinite HF with leak-off in a state of plane strain. This study utilizes a closed form approximate solution of this semi-infinite problem for the fracture width that captures the combined effects of fracture toughness, fluid viscosity, and fluid leak-off. This tip asymptotic solution features a rich multiscale behavior, which strongly depends on the velocity of the crack front. The ILSA scheme developed in this paper makes it possible to account for the three-process multiscale behavior on a structured rectangular mesh by imposing the appropriate asymptotic behavior in tip elements, down to the finest length scale, in a weak sense. To our knowledge this is the first hydraulic fracture simulator capable

to model arbitrarily shaped planar hydraulic fractures that is able to capture, in a rigorous manner, the full three-process multiscale dynamics of the propagating hydraulic fracture. In addition, the methodology developed here for a displacement discontinuity fracture formulation can be utilized to develop multiscale numerical schemes that use alternative representations of fractures.

To validate the multiscale ILSA scheme, firstly, an axisymmetric fracture geometry is considered and the ILSA solutions are compared to reference numerical calculations for a radial hydraulic fracture for a wide range of parameters. Secondly, a sequence of three layer models are considered, in which the three layers correspond to different values of the compressive stress. Results are presented for symmetric stress barriers, asymmetric stress barriers, and a stress drop problem. These results highlight the importance of using the multiscale tip asymptotic solution since different portions of the fracture front propagate at different speeds, so that different asymptotes are used at different points along the fracture boundary in order to locate the moving fracture front. In addition, the results provide reference solutions that can be used to check the performance of other numerical algorithms for modeling a planar hydraulic fracture and to develop more accurate reduced models such as the enhanced P3D model [19].

Acknowledgments

AP acknowledges the support of the British Columbia Oil and Gas Commission and the NSERC discovery grants program (RGPIN-2015-6039). ED acknowledges start-up funds provided by the University of Houston (NRUF, project R110626).

References

[1] D. Spence, D. Turcotte, Magma-driven propagation of cracks, J. Geophys. Res. 90 (1985) 575–580.
[2] D. Spence, P. Sharp, D. Turcotte, Buoyancy-driven crack propagation: a mechanism for magma migration, J. Fluid Mech. 174 (1987) 135–153.
[3] J.R. Lister, Buoyancy-driven fluid fracture: the effects of material toughness and of low-viscosity precursors, J. Fluid Mech. 210 (1990) 263–280.
[4] J.R. Lister, R.C. Kerr, Fluid-mechanical models of crack propagation and their application to magma transport in dykes, J. Geophys. Res. 96 (1991) 10049–10077.
[5] A.M. Rubin, Propagation of magma-filled cracks, Annu. Rev. Earth Planet 23 (1995) 287–336.
[6] S.M. Roper, J.R. Lister, Buoyancy-driven crack propagation: the limit of large fracture toughness, J. Fluid Mech. 580 (2007) 359–380.
[7] E.V. Dontsov, Propagation regimes of buoyancy-driven hydraulic fractures with solidification, J. Fluid Mech. 797 (2016) 1–28.
[8] V.C. Tsai, J.R. Rice, A model for turbulent hydraulic fracture and application to crack propagation at glacier beds, J. Geophys. Res. 115 (2010) F03007.
[9] M.J. Economides, K.G. Nolte (Eds.), Reservoir Stimulation, third ed., John Wiley & Sons, Chichester, UK, 2000.
[10] U. Frank, N. Barkley, Remediation of low permeability subsurface formations by fracturing enhancements of soil vapor extraction, J. Hazard. Mater. 40 (2005) 191–201.
[11] A.S. Abou-Sayed, D.E. Andrews, I.M. Buhidma, Evaluation of oily waste injection below the permafrost in prudhoe bay field, in: Proceedings of the California Regional Meetings, Bakersfield, CA, Society of Petroleum Engineers, Richardson, TX, 1989, pp. 129–142.
[12] R.G. Jeffrey, K.W. Mills, Hydraulic fracturing applied to inducing longwall coal mine goaf falls, in: Pacific Rocks 2000, Balkema, Rotterdam, 2000, pp. 423–430.
[13] S.A. Khristianovic, Y.P. Zheltov, Formation of vertical fractures by means of highly viscous fluids, in: Proc. 4th World Petroleum Congress, vol. 2, 1955, pp. 579–586.
[14] T.K. Perkins, L.R. Kern, Widths of hydraulic fractures, J. Pet. Tech. Trans. AIME (1961) 937–949.
[15] R.P. Nordgren, Propagation of vertical hydraulic fractures, Soc. Petrol. Eng. J. (1972) 306–314.
[16] A. Settari, M.P. Cleary, Development and testing of a pseudo-three-dimensional model of hydraulic fracture geometry (p3dh), in: Proceedings of the 6th SPE Symposium on Reservoir Simulation of the Society of Petroleum Engineers, SPE 10505, 1986, pp. 185–214.
[17] J.D. McLennan, J.C. Picardy, Pseudo-three-dimensional fracture growth modeling, in: 26th US Symposium on Rock Mechanics, 1985, pp. 323–331.
[18] C. Cohen, O. Kresse, X. Weng, A new stacked height growth model for hydraulic fracturing simulation, in: Proceedings 49th U.S. Rock Mechanics Symposium, San Francisco, CA, USA, ARMA-2015-073, American Rock Mechanics Association, 2015.
[19] E. Dontsov, A. Peirce, An enhanced pseudo-3D model for hydraulic fracturing accounting for viscous height growth, non-local elasticity, and lateral toughness, Eng. Fract. Mech. 142 (2015) 116–139.
[20] S.H. Advaniand, T.S. Lee, J.K. Lee, Three-dimensional modeling of hydraulic fractures in layered media: Part I–finite element formulations, J. Energy Resour. Technol. 112 (1990) 1–9.
[21] L. Vandamme, J.H. Curran, A three-dimensional hydraulic fracturing simulator, Internat. J. Numer. Methods Engrg. 28 (1989) 909–927.
[22] A. Peirce, E. Detournay, An implicit level set method for modeling hydraulically driven fractures, Comput. Methods Appl. Mech. Engrg. 197 (2008) 2858–2885.
[23] J. Adachi, E. Siebrits, A. Peirce, J. Desroches, Computer simulation of hydraulic fractures, Int. J. Rock Mech. Min. Sci. 44 (2007) 739–757.
[24] E. Detournay, Mechanics of hydraulic fractures, Annu. Rev. Fluid Mech. 48 (2016) 31139.

[25] J.A.L. Napier, E. Detournay, Propagation of non-planar pressurized cracks from a borehole, in: Research and Applications in Structural Engineering, Mechanics and Computation, 2013, pp. 597–602.
[26] D. Kumar, A. Ghassemi, 3D simulation of multiple fracture propagation from horizontal wells, in: Proceedings 49th U.S. Rock Mechanics Symposium, San Francisco, CA, USA, ARMA-2015-585, American Rock Mechanics Association, 2015.
[27] J.E. Olson, Multi-fracture propagation modeling: Applications to hydraulic fracturing in shales and tight gas sands, in: Proceedings 42nd U.S. Rock Mechanics Symposium, San Francisco, CA, USA, American Rock Mechanics Association, 2008.
[28] A.P. Peirce, A.P. Bunger, Interference fracturing: Non-uniform distributions of perforation clusters that promote simultaneous growth of multiple hydraulic fractures, SPE 172500 (2015) 20.
[29] K. Wu, J. Olson, M.T. Balhoff, W. Yu, Numerical analysis for promoting uniform development of simultaneous multiple fracture propagation in horizontal wells, in: Proceedings of the SPE Annual Technical Conference and Exhibition, SPE-174869-MS, 2015.
[30] O. Kresse, X. Weng, H. Gu, R. Wu, Numerical modeling of hydraulic fracture interaction in complex naturally fractured formations, Rock Mech. Rock Eng. 46 (2013) 555–558.
[31] X. Weng, Modeling of complex hydraulic fractures in naturally fractured formation, J. Unconv. Oil Gas Res. 9 (2015) 114–135.
[32] C.S. Sherman, L.R. Aarons, J.P. Morris, Finite element modeling of curving hydraulic fractures and near- wellbore hydraulic fracture complexity, in: Proceedings 49th U.S. Rock Mechanics Symposium, San Francisco, CA, USA, ARMA-2015-530, American Rock Mechanics Association, 2015.
[33] E. Gordeliy, A.P. Peirce, Implicit level set schemes for modeling hydraulic fractures using the xfem, Comput. Methods Appl. Mech. Engrg. 266 (2013) 125–143.
[34] A.P. Peirce, Implicit level set algorithms for modelling hydraulic fracture propagation, Phil. Trans. R. Soc. A 374 (2016) 20150423.
[35] B. Bourdin, C. Chukwudozie, K. Yoshioka, A variational approach to the numerical simulation of hydraulic fracturing, in: SPE Annual Technical Conference and Exhibition, San Antonio, TX, USA, SPE 159154, Society of Petroleum Engineers, 2012.
[36] A. Mikelic, M.F. Wheeler, T. Wick, Phase-field modeling of a fluid-driven fracture in a poroelastic medium, Comput. Geosci. 19 (2015) 1171–1195.
[37] C. Miehe, S. Mauthe, S. Teichtmeister, Minimization principles for the coupled problem of Darcy–Biot-type fluid transport in porous media linked to phase field modeling of fracture, J. Mech. Phys. Solids 82 (2015) 186–217.
[38] B. Damjanac, C. Detournay, P.A. Cundall, Varun, Three-dimensional numerical model of hydraulic fracturing in fractured rock mass, in: A.P. Bunger, J. McLennan, R. Jeffrey (Eds.), Effective and Sustainable Hydraulic Fracturing, Intech, ISBN: 978-953-51-1137-5, 2013, pp. 819–830. chapter 41.
[39] B. Damjanac, P. Cundall, Application of distinct element methods to simulation of hydraulic fracturing in naturally fractured reservoirs, Comput. Geotech. 71 (2016) 283–294.
[40] H. Ouchi, A. Katiyar, J.T. Foster, M.M. Sharma, A peridynamics model for the propagation of hydraulic fractures in heterogeneous, naturally fractured reservoirs, in: SPE Hydraulic Fracturing Technology Conference, The Woodlands, TX, USA, SPE 173361, Society of Petroleum Engineers, 2015.
[41] J.I. Adachi, E. Detournay, Self-similar solution of a plane-strain fracture driven by a power-law fluid, Int. J. Numer. Anal. Methods Geomech. 26 (2002) 579–604.
[42] E.V. Dontsov, Tip region of a hydraulic fracture driven by a laminar-to-turbulent fluid flow, J. Fluid. Mech. 797 (2016) R2.
[43] E.V. Dontsov, A.P. Peirce, Slurry flow, gravitational settling, and a proppant transport model for hydraulic fractures, J. Fluid Mech. 760 (2014) 567–590.
[44] D.I. Garagash, E. Detournay, J.I. Adachi, Multiscale tip asymptotics in hydraulic fracture with leak-off, J. Fluid Mech. 669 (2011) 260–297.
[45] J. Desroches, E. Detournay, B. Lenoach, P. Papanastasiou, J.R.A. Pearson, M. Thiercelin, A.H.-D. Cheng, The crack tip region in hydraulic fracturing, Proc. R. Soc. Lond. Ser. A Math. Phys. Eng. Sci. 447 (1994) 39–48.
[46] B. Lenoach, The crack tip solution for hydraulic fracturing in a permeable solid, J. Mech. Phys. Solids 43 (1995) 1025–1043.
[47] D. Garagash, E. Detournay, The tip region of a fluid-driven fracture in an elastic medium, J. Appl. Mech. 67 (2000) 183–192.
[48] E. Detournay, D. Garagash, The tip region of a fluid-driven fracture in a permeable elastic solid, J. Fluid Mech. 494 (2003) 1–32.
[49] E. Dontsov, A. Peirce, A non-singular integral equation formulation to analyze multiscale behaviour in semi-infinite hydraulic fractures, J. Fluid. Mech. 781 (2015) R1.
[50] E.V. Dontsov, A.P. Peirce, Incorporating viscous, toughness, and intermediate regimes of propagation into enhanced pseudo-3D model, in: Proceedings 49th U.S. Rock Mechanics Symposium, San Francisco, CA, USA, ARMA-2015-297, American Rock Mechanics Association, 2015.
[51] A.P. Peirce, Modeling multi-scale processes in hydraulic fracture propagation using the implicit level set algorithm, Comput. Methods Appl. Mech. Engrg. 283 (2015) 881–908.
[52] M.V. Madyarova, Fluid-driven penny-shaped fracture in elastic medium (Ph.D. thesis), University of Minnesota, 2003.
[53] J.R. Rice, Mathematical analysis in the mechanics of fracture, in: H. Liebowitz (Ed.), in: Fracture: An Advanced Treatise, vol. II, Academic Press, New York, NY, 1968, pp. 191–311 (Chapter 3).
[54] E.D. Carter, Optimum fluid characteristics for fracture extension, in: G.C. Howard, C.R. Fast (Eds.), Drilling and Production Practices, 1957, pp. 261–270.
[55] A.P. Bunger, E. Detournay, Early time solution for a penny-shaped hydraulic fracture, ASCE J. Engrg. Mech. 133 (2007) 175–190.
[56] E. Detournay, A. Peirce, On the moving boundary conditions for a hydraulic fracture, Internat. J. Engrg. Sci. 84 (2014) 147–155.
[57] A.P. Peirce, E. Siebrits, The scaled flexibility matrix method for the efficient solution of boundary value problems in 2D and 3D layered elastic media, Comput. Methods Appl. Mech. Engrg. 190 (2001) 5935–5956.
[58] A.P. Peirce, E. Siebrits, Uniform asymptotic approximations for accurate modeling of cracks in layered elastic media, Int. J. Fract. 110 (2001) 205–239.
[59] E. Siebrits, A.P. Peirce, An efficient multi-layer planar 3D fracture growth algorithm using a fixed mesh approach, Internat. J. Numer. Methods Engrg. 53 (2002) 691–717.

[60] S.L. Crouch, A.M. Starfield, Boundary Element Methods in Solid Mechanics, George Allen and Unwin, London, 1983.
[61] D.A. Hills, P.A. Kelly, D.N. Dai, A.M. Korsunsky, Solution of crack problems, The Distributed Dislocation Technique, Solid Mechanics and its Applications, vol. 44, Kluwer Academic Publisher, Dordrecht, 1996.
[62] A.P. Peirce, E. Siebrits, A dual mesh multigrid preconditioner for the efficient solution of hydraulically driven fracture problems, Internat. J. Numer. Methods Engrg. 63 (2005) 1797–1823.
[63] A.P. Peirce, Localized jacobain ILU preconditioners for hydraulic fractures, Internat. J. Numer. Methods Engrg. 65 (2006) 1935–1946.
[64] J.A. Sethian, Level Set Methods and Fast Marching Methods: Evolving interfaces in Computational Geometry Fluid Mechanics Computer Vision and Materials Science, Cambridge University Press, Cambridge, UK, 1999.
[65] S. Osher, R. Fedkiw, Level Set Methods and Dynamic Implicit Surfaces, Vol. 153, Springer-Verlag, New York, 2002.
[66] J.I. Adachi, E. Detournay, A.P. Peirce, An analysis of classical pseudo-3D model for hydraulic fracture with equilibrium height growth across stress barriers, Int. J. Rock Mech. Min. Sci. 47 (2010) 625–639.